Improving Landsat land surface temperature estimation in Google Earth Engine using NDVI-based emissivity

Hana Bobáľováa*, Šimon Opravilb

- a Comenius University in Bratislava, Faculty of Natural Sciences, *Department of Physical Geography and Geoinformatics, Mlynská Dolina, Ilkovičova 6, 84215 Bratislava, Slovakia*
 - b Slovak Academy of Sciences, Institute of Geography, Štefánikova 49, 814 73 Bratislava, Slovakia

Abstract

1

2

3

4

5

6

7

8

9

10

11

12

13

14

15

16

17

18

19

20

21

22

23

24

25

26

27

3132

33 34

35

36

37

38

39

40

41

42

43

44

Land surface temperature (LST) data derived from satellite images are important for various applications, including mapping urban heat islands, analysing temporal and spatial temperature patterns, assessing the cooling effect of urban greenery, and developing population vulnerability indices for heat waves. Thermal sensors aboard Landsat satellites provide the most spatially detailed data with the longest temporal continuity. Although Landsat Surface Temperature (ST) is already available as a standard product, and a code for estimating the Landsat LST using the statistical monowindow method has been implemented in the Google Earth Engine, these approaches rely on the ASTER Global Emissivity Dataset, which has certain limitations, including missing values. In Google Earth Engine, we developed an approach to calculate land surface emissivity using various NDVI-based methods, combined with the statistical mono-window and radiative transfer equation methods for LST calculation. Validation against in situ measurements from the SURFRAD network revealed that the statistical mono-window method proved to be more accurate than the Landsat ST product and radiative transfer equation methods, regardless of the emissivity data source. The NDVI-based emissivity combined with the statistical mono-window method yielded higher LST precision than the approach using ASTER GED emissivity. These results were consistent across all Landsat missions. Furthermore, we demonstrate that the lowest accuracy is achieved in calculating LST on mixed surfaces and the highest on bare soil. The overestimation of satellite LST measurements at high temperatures was only apparent on mixed and vegetated surfaces, while it was more pronounced in the Landsat ST product and other radiative transfer equation methods. These findings and the publicly available Google Earth Engine code can lead to more accurate LST mapping and analysis results.

- 28 **Keywords:** Land surface temperature; Landsat; Google Earth Engine; Land surface emissivity; NDVI
- 29 This manuscript is a non-peer-reviewed preprint submitted to EarthArXiv (October, 2025).
- 30 Manuscript is currently under review in Advances in Space Research Journal.

1. Introduction

Land surface temperature (LST) is a critical parameter for understanding environmental processes such as urban heat islands (UHIs), climate dynamics, and ecosystem responses to global warming. Derived from satellite thermal infrared data, LST enables applications like mapping urban heat patterns, analyzing temporal and spatial temperature trends, assessing the cooling effects of urban greenery, and developing vulnerability indices for heatwaves. As global warming intensifies, with a projected increase of at least 1.5°C in coming decades (IPCC, 2021), the frequency and severity of heatwaves have escalated. Concurrently, rapid urbanization has driven the global urban population from 29% in 1950 to 55% in 2018, with projections reaching 68% by 2050, predominantly in Asia and Africa (UN, 2019). In urban areas, this combination amplifies UHIs, where built-up regions exhibit significantly higher temperatures than surrounding rural areas (Voogt and Oke, 2003), increasing health risks for vulnerable populations such as the elderly and those with cardiorespiratory conditions (Arsad et al., 2022).

To study these phenomena, many algorithms have been developed to calculate LST from thermal infrared images (Li et al., 2013a, 2023; Mohamed et al., 2016). Single-channel methods use only one thermal infrared band to calculate LST but require several additional parameters. The simplest method involves inverting the radiative transfer equation, which necessitates prior knowledge of land surface emissivity and atmospheric parameters such as transmissivity, upwelling radiance, and downwelling radiance. These parameters are also required for the single-channel algorithm revised by Jiménez-Muñoz et al. (2009). The mono-window algorithm developed by Qin et al. (2001) requires three main parameters: land surface emissivity, atmospheric transmissivity, and effective mean atmospheric temperature. Split-window algorithms retrieve LST by leveraging the differential atmospheric absorption in two adjacent TIR channels to correct for atmospheric effects, which also requires knowledge of the land surface emissivity in both channels. Additionally, LST and land surface emissivity can be determined simultaneously using the multi-channel algorithms like the Temperature and emissivity separation (TES) (Gillespie et al., 1998) or Temperature independent spectral index (TISI) (Becker and Li, 1990). Land surface emissivity is a crucial parameter for retrieving accurate LST from satellite imagery. Besides the multi-channel approaches, land surface emissivity can be determined using semi-empirical methods based on typical emissivity values for different land cover classes (classification-based emissivity method) (Snyder et al., 1998), or based on the relationship between land surface emissivity and the normalized difference vegetation index NDVI (NDVI-based emissivity method) (Sobrino and Raissouni, 2000; Valor and Caselles, 1996; van de Griend and Owe, 1993). The Advanced Spaceborne Thermal Emission and Reflection Radiometer Global Emissivity Dataset (ASTER GED) is also frequently used as a source of emissivity data (Hulley et al., 2015). This dataset consists of LST and land surface emissivity values calculated by the TES algorithm for all cloud-free pixels from ASTER satellite scenes collected between 2000 and 2008. However, the dataset contains areas with missing mean emissivity data, leading to gaps in the resulting LST products. In some cases, block artefacts or vegetation adjustment anomalies may occur in areas where significant changes in NDVI have occurred since the

2000-2008 (USGS, n.d.).

LST data is also available as a ready-made product from various satellites (MODIS, VIIRS, Sentinel-3). Recently, ST products from individual Landsat satellite missions have also become available (Cook et al., 2014). The Landsat series offers a long temporal continuity of imaging, starting from the 1970s-80s, similar to meteorological satellites. Landsat TIR sensors, with the highest spatial resolution among thermal satellite sensors (60-120 m, resampled to 30 m), provide data suitable for Surface Urban Heat Island analysis at regional or local scales. The Landsat ST product is calculated using the radiative transfer equation single-channel method, which utilizes atmospheric profiles and additional data, including ASTER GEDv3 (Malakar et al., 2018; USGS, 2021).

Before the availability of Landsat ST products, several solutions were developed to automate LST calculation. For instance, the web application developed by Parastatidis et al. (2017) (https://rslab.gr/Landsat_LST.html) applies the single-channel algorithm method based on statistical simulations with various atmospheric profile inputs, leading to a convenient equation for global LST calculation (Jiménez-Muñoz et al., 2009, 2014). Software tools for automated Landsat LST derivation have also been developed in widely used geographic information systems like ArcGIS (Sekertekin and Bonafoni, 2020a) or QGIS (Ndossi and Avdan, 2016), offering several algorithms for LST calculation.

The use of web applications, software plugins, or ready-made Landsat ST products can become cumbersome when analysing larger areas or longer time series, as they require downloading and processing large volumes of data. To address this, Ermida et al. (2020) developed a code repository for calculating LST from Landsat images within the Google Earth Engine environment. Google Earth Engine (GEE) is a cloud platform for planetary-scale geospatial analysis, offering petabyte-scale archives of remote sensing data (Gorelick et al., 2017). It provides access to high-performance computing resources for processing large geospatial datasets through a JavaScript IDE or via JavaScript and Python APIs. Ermida et al. (2020) utilized a statistical mono-window algorithm, originally developed for

deriving LST from Meteosat satellites (Duguay-Tetzlaff et al., 2015). This approach is based on a linear regression relationship between brightness, temperature and LST, simulated for different classes of atmospheric water vapour. However, the statistical mono-window implementation in Google Earth

98 Engine also utilizes ASTER GEDv3.

99

100

101

102

103

104

105

106

107

108

109

110

111

112

113

114

115

116

117

118

119

120

121

122

126

Several studies have focused on validating the accuracy of different methods for calculating Landsat LST. Parastatidis et al. (2017) assessed Landsat LST accuracy by comparing it with ASTER LST products and analysing different land surface emissivity sources. Ndossi and Avdan (2016) compared satellite LST with near-surface air temperatures from meteorological stations. However, the standard approach involves comparing satellite LST with in situ data from networks equipped with ground-based radiometers, such as the Surface Radiation Budget Network (SURFRAD) in the USA, or the worldwide Baseline Surface Radiation Network (BSRN) (Duan et al., 2019; Guillevic et al., 2018; Martin et al., 2019). Landsat LST validation was limited to a few or several dozen measurements in the past due to the need to download satellite scenes (Sekertekin and Bonafoni, 2020a; Yu et al., 2014). Today, the Google Earth Engine platform enables validation using the entire available set of cloud-free Landsat scenes (Ermida et al., 2020).

To address the issues with the ASTER GEDv3 product and provide alternatives to existing Landsat LST products and calculation methods, we developed a Google Earth Engine code that:

- 1. estimates land surface emissivity using the NDVI-based method,
- 2. calculates land surface temperature using the radiative transfer equation (RTE) method, and
- 3. allows the use of NDVI-based emissivity in the statistical mono-window (SMW) LST calculation proposed by Ermida et al. (2020).

We demonstrate the application of this code in Bratislava, the capital of Slovakia, an area where ASTER GEDv3 values are missing. Validation of the proposed methods using in-situ measurements from the SURFRAD network enabled us to evaluate accuracy of different LST calculation approaches, specifically:

- 1. the empirical SMW method versus the RTE method,
- 2. the use of ASTER-based versus NDVI-based emissivity (and the impact of different NDVI thresholds), and
- 3. the accuracy of LST retrieval over bare soil, vegetated surfaces, and mixed land cover types.
- 123 We hope that the findings of this study can contribute to improving LST retrieval from Landsat
- imagery and enhancing subsequent environmental and climate-related analyses.

125 **2. Data**

2.1. Landsat Data

- The GEE catalogue includes Landsat Collection 2 data, which offers enhanced radiometric consistency and improved geolocation for time series analyses compared to the older Collection 1 (Crawford et al.,
- 2023). For the calculation of LST and land surface emissivity, we use Tier 1 data, which are of the
- 130 highest quality. Table 1 summarises the datasets used for various Landsat missions. Landsat 4-5
- Thematic Mapper (TM) and Landsat 7 Enhanced Thematic Mapper (ETM+) sensors capture data in the
- visible and infrared spectrum. The Landsat 8-9 Operational Land Imager (OLI) sensor records radiation
- in the visible and shortwave infrared, while the Thermal Infrared Sensor (TIRS) records in the thermal
- infrared spectrum. The TM sensor provides thermal band B6 at a resolution of 120 metres, whereas
- for the ETM+ sensor, we used the low-gain version of thermal band B6 at a resolution of 60 metres
- due to its larger dynamic range. Band 10 was selected for the TIRS sensor, as band B11 has a greater
- calibration uncertainty (Malakar et al., 2018). All thermal bands were resampled to 30 metres by USGS
- to match the spatial resolution of the other spectral bands.
- The Top of Atmosphere (TOA) dataset represents calibrated reflectance at the top of the atmosphere
- and is used to calculate LST using the statistical mono-window method. For the LST calculation using
- the radiative transfer equation method, we employ the raw image dataset (DN) representing Level-1
- 142 Precision Terrain (L1TP) data, which can then be converted to calibrated at-sensor radiance. The

Surface Reflectance (SR) dataset contains atmospherically corrected surface reflectance. It is used to calculate the Normalised Difference Vegetation Index (NDVI) from red and near infrared bands at a spatial resolution of 30 metres. From this dataset, we also used intermediate bands of upwelling radiance (ST_URAD), downwelling radiance (ST_DRAD), and atmospheric transmittance (ST_ATRAN) to calculate LST using the radiative transfer equation method. Additionally, we obtained the ST band from the same dataset. In some cases, the assets include only SR data, where the ST band may be present but empty.

150 Table 1. Datasets of Landsat satellite missions used to calculate the LST in Google Earth Engine.

Name	GEE Dataset	Date Range							
Landsat 4									
SR	LANDSAT/LT04/C02/T1_L2								
TOA	LANDSAT/LT04/C02/T1_TOA	August 1982 – December 1993							
DN	LANDSAT/LT04/C02/T1								
Landsat 5									
SR	LANDSAT/LT05/C02/T1_L2								
TOA	LANDSAT/LT05/C02/T1_TOA	March 1984 – May 2012							
DN	LANDSAT/LT05/C02/T1								
Landsat 7									
SR	LANDSAT/LE07/C02/T1_L2								
TOA	LANDSAT/LE07/C02/T1_TOA	January 1999 – April 2022							
DN	LANDSAT/LE07/C02/T1								
Landsat 8									
SR	LANDSAT/LC08/C02/T1_L2								
TOA	LANDSAT/LC08/C02/T1_TOA	April 2013 – Present							
DN	LANDSAT/LC08/C02/T1/								
Landsat 9									
SR	LANDSAT/LC09/C02/T1_L2								
TOA	LANDSAT/LC09/C02/T1_TOA	October 2021 – Present							
DN	LANDSAT/LC09/C02/T1								
SR = Surfac	e Reflectance								
TOA = Top	TOA = Top of Atmosphere reflectance								
DN = DN va	llues (at-sensor radiance)								

2.2. Surface Radiation Data

The calculated LST was compared with in situ data from the SURFRAD radiation network, established in the USA in the 1990s to support modern climate and hydrological research (Augustine et al., 2000). The network currently consists of six stations (Fig. 1), which primarily measure the downwelling and upwelling components of broadband solar and thermal infrared irradiance. Data are recorded at one-minute interval, and measurements were selected to match the Landsat image acquisition time. For LST validation, upwelling and downwelling infrared radiances are measured with pyrgeometers at a spatial resolution of 70 x 70 metres, with an accuracy of approximately 5 W/m². All SURFRAD stations are part of the Baseline Surface Radiation Network (BSRN), a project of the World Climate Research Programme (WCRP). Data from the SURFRAD stations have been used to validate LST derived from Landsat (Duan et al., 2021; Malakar et al., 2018), MODIS (Duan et al., 2019), or VIIRS (Liu et al., 2022, 2015).

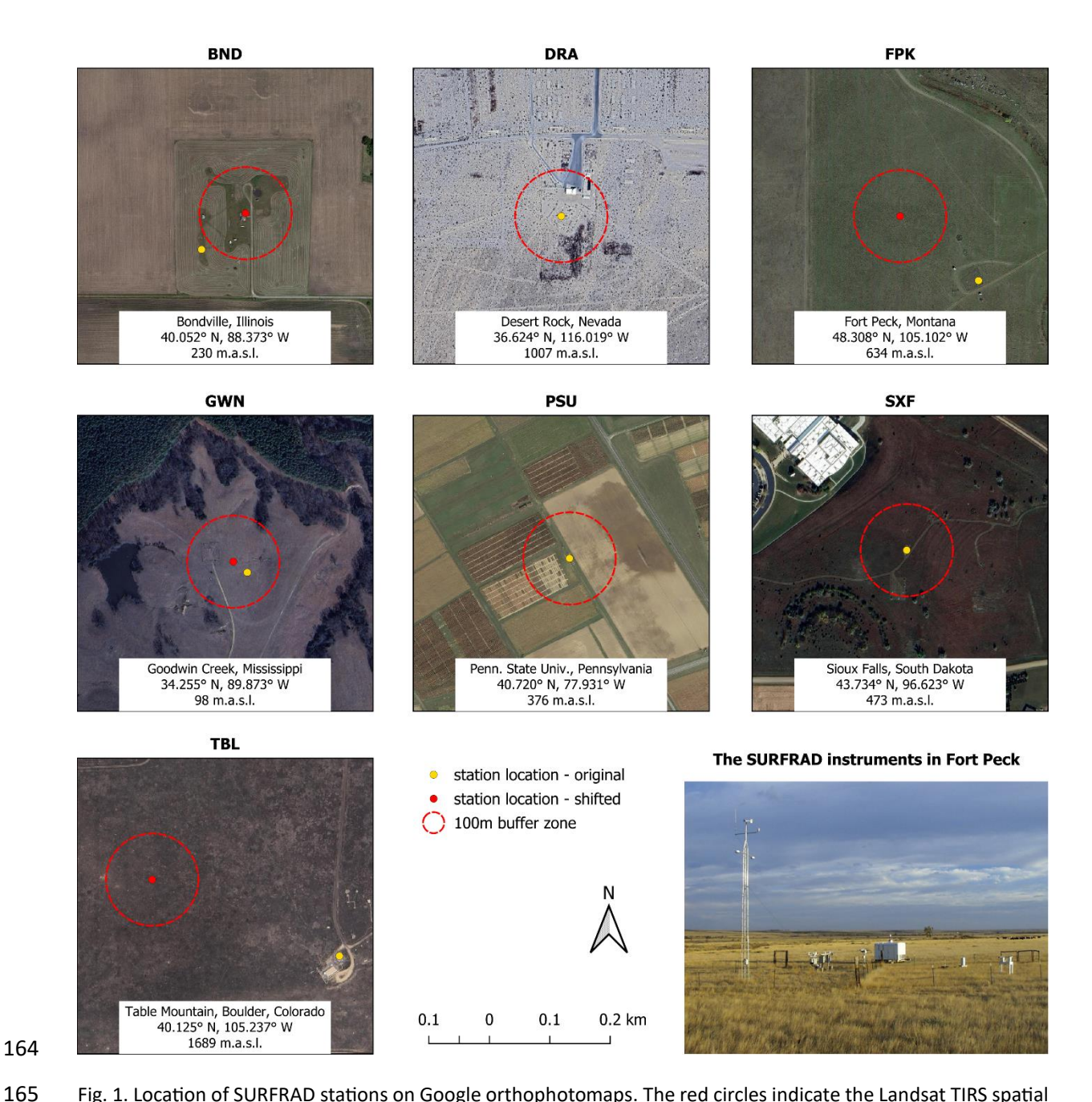


Fig. 1. Location of SURFRAD stations on Google orthophotomaps. The red circles indicate the Landsat TIRS spatial resolution (100m radius). For some stations, locations are slightly shifted to obtain data from more homogeneous surface, following the approach used in Ermida et al. (2020).

3. Methods

3.1. LST retrieval methods

3.1.1. Radiative transfer equation method

We developed a code to calculate LST using the radiative transfer equation method in the Google Earth Engine environment. This method uses a single thermal band, making it applicable to data from Landsat 4-9 satellites. Unlike the mono-window algorithm, the radiative transfer equation method does not require knowledge of the effective mean atmospheric temperature. Instead, it employs the inversion

of the Radiative Transfer Equation to compute ground radiance from at-sensor (TOA) radiance (Dash et al., 2001):

$$L_{\lambda} = \tau \varepsilon B_{\lambda}(T_S) + L_{\lambda}^{\uparrow} + \tau (1 - \varepsilon) L_{\lambda}^{\downarrow} \tag{1}$$

- where $B_{\lambda}(T_S)$ is the radiance of a blackbody target of surface temperature T_S (ground radiance), L_{λ}^{\uparrow} is the upwelling or atmospheric path radiance, L_{λ}^{\downarrow} is the downwelling or sky radiance, τ is atmospheric transmittance, ε is land surface emissivity. Radiances are in units of W/m²·sr·µm and transmittance and emissivity are unitless.
- The radiative transfer equation describes TOA radiance as a combination of surface radiance 182 183 attenuated by the atmosphere, atmospheric contribution along the upward path (upwelling radiance), and atmospheric radiance reflected by the surface and attenuated along the upward path 184 185 (downwelling radiance). Upwelling radiance, downwelling radiance and transmittance have been 186 routinely obtained since 2003 from the Atmospheric Correction Parameter Calculator (Barsi et al., 187 2003), which used atmospheric profiles from the National Centres for Environmental Prediction (NCEP) and the commercially available MODTRAN software. As of January 1, 2024, this tool has been 188 discontinued, as intermediate image products of the upwelling and downwelling radiance and 189
- TOA spectral radiance (LTOA) is derived from the calibrated digital number (DN) values of the Landsat Level-1 thermal band using the radiance rescaling factors provided in the scene metadata file:

transmittance from Landsat Collection 2 Level-2 Science Products are now available.

$$L_{\lambda} = M_L Q_{CAL} + A_L \tag{2}$$

- where M_L is the band-specific multiplicative rescaling factor from the metadata, A_L is the band-specific additive rescaling factor from the metadata, and Q_{cal} is the quantised and calibrated standard product pixel values (DN). In Google Earth Engine, this calculation can be performed using the Landsat.calibratedRadiance algorithm.
- By inverting Eq. (1), we can obtain the blackbody radiance at a given surface temperature $B_{\lambda}(T_S)$ from LTOA:

$$B_{\lambda}(T_S) = \frac{L_{\lambda} - L_{\lambda}^{\uparrow} - \tau(1 - \varepsilon)L_{\lambda}^{\downarrow}}{\tau \varepsilon}$$
(3)

Subsequently, the surface temperature T_S (LST) can be derived by inverting Planck's law or using the Landsat-specific estimation of the Planck curve:

$$T_S = \frac{K_2}{\ln\left(1 + \frac{K_1}{B_\lambda(T_S)}\right)} \tag{4}$$

- where K_1, K_2 are thermal calibration constants (available in metadata files).
- The operational algorithm for calculating the Landsat ST product also includes atmospheric corrections using the radiation transfer model. However, this algorithm is more complex and employs a lookup table approach instead of the less accurate inversion of the Planck function. This algorithm was developed at the Rochester Institute of Technology and NASA Jet Propulsion Laboratory in collaboration with USGS software engineers (Malakar et al., 2018; USGS, 2021).

3.1.2. Statistical mono-window method

190

207

208 Ermida et al. (2020) employed the Statistical Mono-Window algorithm, developed by the Climate 209 Monitoring Satellite Application Facility (CM-SAF) to derive LST climate data records from Meteosat 210 First and Second Generation (MFG and MSG) satellites. This algorithm is straightforward to calibrate and implement, as it relies on a simple linear regression between the LST and the TOA brightness

212 temperature in a single TIR channel:

$$LST = A_i \frac{Tb}{\varepsilon} + B_i \frac{1}{\varepsilon} + C_i \tag{5}$$

where Tb is the TOA brightness temperature in the TIR channel, and ε is the surface emissivity for the

same channel. The algorithm's coefficients A_i , B_i , C_i are determined from linear regressions of

radiative transfer simulations performed for 10 classes of Total Column Water Vapour.

3.2. Land surface emissivity retrieval methods

217 3.2.1. ASTER GEDv3 emissivity

218 Several algorithms for calculating LST require prescribed surface emissivity values. Emissivity at a given

- 219 wavelength λ and temperature T is defined as the ratio of radiance $L_{\lambda}(T)$ emitted by a body at
- temperature T to the radiance $B_{\lambda}(T)$ emitted by a black body at the same temperature (Li et al.,
- 221 2013b):

216

$$\varepsilon_{\lambda}(T) = \frac{L_{\lambda}(T)}{B_{\lambda}(T)} \tag{6}$$

222 Since 2014, the global product ASTER GEDv3 has been available, providing emissivity for five ASTER TIR

223 bands at resolutions of 100 m and 1 km. This dataset, derived from cloud-free ASTER images taken

- between 2000 and 2008, has a reported emissivity accuracy of approximately 1%. It is used in the
- production of Landsat ST layers and in the statistical mono-window method coded by Ermida et al.
- 226 (2020). However, since 2008, significant changes in land cover and seasonal variations in vegetation
- 227 may have occurred in some areas. Therefore, it is recommended to correct ASTER GED emissivity based
- on the NDVI, where the fractional vegetation cover (FVC) is first calculated (Carlson and Ripley, 1997):

$$FVC = \left(\frac{NDVI - NDVI_S}{NDVI_V - NDVI_S}\right)^2 \tag{7}$$

229 where NDVI_V and NDVI_S represent pixels fully covered by vegetation and bare soil, respectively. To

obtain consistent FVC values, the FVC is set to zero for pixels with NDVI < NDVI_s and set to one for pixels

- 231 with NDVI > NDVI_V (Sobrino et al., 2008).
- 232 The emissivity is then adjusted using an equation:

$$\varepsilon = FVC\varepsilon_V + (1 - FVC)\varepsilon_S \tag{8}$$

where ε_V and ε_S represent the emissivity of vegetation and bare soil for a given spectral band, with

234 ε_V determined as a constant, and ε_S derived from the original ASTER emissivity data (Ermida et al.,

235 2020; Malakar et al., 2018).

236

246

3.2.2. NDVI-based emissivity

237 One drawback of using the ASTER GEDv3 dataset, including its NDVI-corrected modifications, is the

238 presence of missing values and artefacts in certain areas. As an alternative, classification-based

emissivity methods and NDVI-based emissivity methods can be used for single-channel LST calculation

240 methods (Li et al., 2013b). Classification-based emissivity methods are demanding in terms of input

data, as they require land cover classification and the subsequent assignment of typical emissivity

values to land cover classes. For this reason, classification-based emissivity methods are less frequently

used in practice compared to NDVI-based emissivity methods, which includes methods such as the

244 NDVI-threshold method (NDVI^{THM}) (Sobrino and Raissouni, 2000), simplified NDVI^{THM} (SNDVI^{THM})

(Sobrino et al., 2008), improved NDVI^{THM} (INDVI^{THM}) (Tang et al., 2015), and a new method for separate

emissivity calculation for vegetated and non-vegetated surfaces (Cheng et al., 2021). In our Google

- Earth Engine code, we used the NDVI^{THM} and SNDVI^{THM} methods due to their straightforward implementation for Landsat 4-9 satellite images.
- 249 The NDVI^{THM} method uses FVC to calculate the emissivity of mixed surfaces, while the emissivity of
- bare soil pixels (NDVI < NDVI_s) is estimated from the reflectance in the red band, and pixels fully
- covered by vegetation (NDVI > NDVI_V) acquire a constant emissivity value (Sobrino and Raissouni,
- 252 2000):

$$\varepsilon = a_i \rho_{RED} + b_i \qquad NDVI < NDVI_S$$

$$\varepsilon = \varepsilon_V FVC + \varepsilon_S (1 - FVC) + C_i \qquad NDVI_S \le NDVI_V \qquad (9)$$

$$\varepsilon = \varepsilon_V + C_i \qquad NDVI > NDVI_V$$

253 where C_i is a term which takes the cavity effect into account due to the surface roughness ($C_i = 0$ for flat surfaces). The cavity term for a mixed area and near-nadir view is given by (Sobrino et al., 2004):

$$C_i = (1 - \varepsilon_S)\varepsilon_V F'(1 - FVC) \tag{10}$$

- 255 where F' is a geometrical factor ranging between zero and one, depending on the geometrical distribution of the surface, with a typical mean value of 0.55.
- Due to the discontinuity of the emissivity values at NDVI = NDVI_S and NDVI = NDVI_V, Sobrino et al. (2008)
- 258 proposed an alternative method, SNDVI^{THM}, which does not consider the cavity term and sets a
- 259 constant for pixels of bare soil:

$$\varepsilon = \varepsilon_{S}$$
 NDVI < NDVI_S

$$\varepsilon = \varepsilon_{S}FVC + (\varepsilon_{V} - \varepsilon_{S})FVC$$
 NDVI_S \leq NDVI \leq NDVI_V (11)
$$\varepsilon = \varepsilon_{V}$$
 NDVI > NDVI_V

- Both methods require prior knowledge of the emissivity values of vegetation and bare soil, which are typically derived from various spectral libraries such as ASTER, MODIS or ECOSTRESS.
- In addition to the ε_s and ε_V values, another source of uncertainty in LST calculations is the selection of
- 263 the NDVI_S and NDVI_V thresholds, which also influence the calculation of FVC. Sobrino and Raissouni
- 264 (2000) proposed threshold values of $NDVI_S = 0.2$ and $NDVI_V = 0.5$ for global applications, which have
- been widely adopted in subsequent studies (Ndossi and Avdan, 2016; Sekertekin and Bonafoni, 2020a;
- Sobrino et al., 2008; Yu et al., 2014). However, Jiménez-Muñoz et al. (2009) suggested that the NDVIv
- threshold of 0.5 is suitable only for low-resolution image data, recommending a higher threshold value
- of around 0.85 for high resolution data. This recommendation has been followed by authors such as
- 269 Parastatidis et al. (2017), Ren et al. (2017), and Ermida et al. (2020).
- 270 The accuracy of the LST calculation using various NDVI^{THM} methods was validated by Sekertekin and
- 271 Bonafoni (2020) on a limited sample of Landsat images through a comparison with in situ data from
- the SURFRAD network. The Google Earth Engine platform allows for the use of the entire Landsat image
- archive for validation. We selected three NDVI^{THM} methods (the first three most accurate methods
- according to Sekertekin and Bonafoni, 2020) and three SNDVI^{THM} methods (Table 2) to evaluate the
- accuracy of the LST derived from the cloud-free Landsat 8 scenes. We developed a code in Google
- 276 Earth Engine to calculate the land surface emissivity using these methods. The land surface emissivity
- 277 is then used in deriving the LST using the radiative transfer equation and statistical mono-window
- 278 methods. We used threshold values of NDVIS = 0.2 and NDVIV = 0.5 for the initial settings.
- Furthermore, we tested a higher threshold value of $NDVI_V = 0.85$ at selected stations with vegetated
- surfaces (BND, PSU, GWN, FPK, and SXF). We tested 48 variants of land surface emissivity calculation
- using the Landsat 8 archive.

287

288

289

290

291

292

293

294

295

296

Method	Reference			Spectral	
Wethou	Reference	NDVI < NDVIs	$NDVI_S < NDVI < NDVI_V$	$\textbf{NDVI}_{\textbf{V}}$	library
NDVI ^{THM} SO	Sobrino et al. (2008)	0.979 – 0.035ρ _{RED}	0.986 + 0.004FVC	0.99	ASTER
NDVI ^{THM} SK	Skoković et al. (2014)	$0.979-0.046\rho_{RED}$	0.987FVC + 0.971(1 - FVC)	0.99	ASTER
$NDVI^THM\;YU$	Yu et al. (2014)	$0.973-0.047\rho_{RED}$	$0.9863FVC + 0.9668(1 - FVC) + C_i$	0.9863 + C _i	MODIS
SNDVI ^{THM} SK	ε _S , ε _V from Skoković et al. (2014)	0.971	0.971 + (0.987 – 0.971)FVC	0.987	ASTER
SNDVI ^{THM} YU	ε _S , ε _V from Yu et al. (2014)	0.9668	0.9668 + (0.9863 - 0.9668)FVC	0.9863	MODIS
SNDVI ^{THM} WA	ε _S , ε _V from Wang et al. (2015)	0.966	0.966 + (0.973 - 0.966)FVC	0.973	ASTER

NDVI^{THM} – NDVI threshold method SNDVI^{THM} – Simplified NDVI threshold method NDVIs, NDVIv – threshold values for bare soil and vegetation ϵ_S , ϵ_V – emissivity of bare soil and vegetation FVC – Fractional Vegetation Cover C_i – cavity term

The Google Earth Engine code for calculating LST was written in Javascript in the Code Editor environment. The scripts enable the calculation of LST by the radiative transfer equation method in combination with NDVI-based emissivity methods. Furthermore, we have added the option of NDVI-based emissivity methods to the scripts for LST calculation using the statistical mono-window method by Ermida et al. (2020). The code is available from the Google Earth Engine or GitHub repositories:

- https://code.earthengine.google.com/?accept_repo=users/hanabobalova/LST_Landsat
- https://github.com/hanabobalova/GEE Landsat LST.git

3.3. Validation against in situ measurements

The instruments at SURFRAD stations measure longwave infrared downwelling and upwelling radiation in the range of 4-50 μ m (Augustine et al., 2000). For broadband measurements, in situ LST is related to surface longwave radiation by the Stefan-Boltzmann law (Wang and Liang, 2009):

$$LST = \sqrt[4]{\frac{L_{\lambda}^{\uparrow} - (1 - \varepsilon_B)L_{\lambda}^{\downarrow}}{\varepsilon_B \sigma}}$$
 (12)

- where ε_B is the broadband emissivity of the surface and σ is the Stefan-Boltzmann constant.
- Broadband emissivity at each station can be estimated from the narrowband emissivities of the ASTER GEDv3 product using the following regression relationship (Ermida et al., 2020; Malakar et al., 2018):

$$\varepsilon_B = 0.128 + 0.014\varepsilon_{A10} + 0.145\varepsilon_{A11} + 0.241\varepsilon_{A12} + 0.467\varepsilon_{A13} + 0.004\varepsilon_{A14}$$
 (13)

- 300 where ε_{A10} to ε_{A14} denote the ASTER emissivities in bands 10 to 14.
- We compared in situ LST measurements with satellite-derived LST and calculated the root mean square error (RMSE) for each method and SURFRAD station:

$$RMSE = \sqrt{\frac{\sum_{i=1}^{n} (LST_{satellite} - LST_{insitu})}{n}}$$
 (14)

- 303 where $LST_{satellite}$ and LST_{insitu} are the satellite and in situ LSTs, respectively, and n denotes the number of observations.
- 305 However, the Committee on Earth Observation Satellites Working Group (CEOS) on Calibration and
- 306 Validation (Guillevic et al., 2018) recommends the use of robust statistics for the validation of LST
- 307 products, characterised by the median error μ (also known as accuracy):

$$\mu = median(LST_{satellite} - LST_{insitu}) \tag{15}$$

The robust equivalent of the standard deviation (SD) is known as precision σ , given by the median of absolute differences:

$$\sigma = median(|LST_{satellite} - LST_{insitu}| - \mu)$$
(16)

310 Since the first SURFRAD stations began measuring in 1994, no validation measurements were available 311 for Landsat 4 satellite images. For validation, we selected all Tier 1 images from Landsat 5 to 9 satellites with a cloud cover of 10% or less. Only the first scene was selected when overlapping scenes were 312 313 captured on the same acquisition date (at DRA, FPK, and SXF stations). Despite the cloud cover 314 threshold, a significant number of outliers with much lower LST were observed, indicating cloud 315 contamination. To exclude potential outliers, we applied the robust "3o-Hampel identifier" method 316 (Davies and Gather, 1993; Duan et al., 2019). Unlike the common method of removing values more 317 than 3 SD from the mean, this approach replaces the mean with the median and calculates the SD as 318 follows:

$$SD = 1.4826 \times median\{|(LST_{satellite} - LST_{insitu}) - \mu|\}$$
(17)

We applied the removal of outliers to the entire data sequence at once because different bias at the stations would lead to significantly different threshold values if removal were done on a per-station basis. Additionally, we did not apply outlier removal separately for each method because we aimed to compare their accuracy using a uniform set of measurements. We selected the statistical monowindow method from Ermida et al. (2020) as the base method for the SD calculation, as it provided better preliminary results than the Landsat ST product.

4. Results

- We applied our methods to generate LST maps for Bratislava, Slovakia, using a Landsat 8 scene from July 22, 2022 (Fig. 2). Located in a temperate continental climate with urban, agricultural, and riverine features, Bratislava exemplifies regions with incomplete ASTER GEDv3 coverage, along with other cities such as Olomouc (Czech Republic), Bordeaux (France) or Toronto (Canada). The resulting maps revealed peak LST values in industrial zones and bare arable land (up to 318 K), contrasting with cooler areas near the Danube River and vegetated zones. This showcases the capability of our GEE code to produce high-resolution LST datasets where traditional emissivity sources falter.
- We evaluated three LST retrieval methods—Landsat ST (USGS product), statistical mono-window (SMW), and radiative transfer equation (RTE)—against SURFRAD in-situ measurements across 882 Landsat 8 scenes, after excluding 7.2% outliers via a robust 3σ-Hampel filter (Table 3). SMW consistently outperformed both alternatives, regardless of the emissivity source. With ASTER GEDv3, SMW achieved RMSE of 2.58 K, compared to 3.61 K for Landsat ST and 3.40-3.75 K for RTE. SMW also exhibited minimal bias (0.25 K with ASTER) and higher precision (1.36 K) than RTE (Table S1). Landsat ST and RTE methods tend to produce slightly higher LST compared to SMW resulting in positive bias

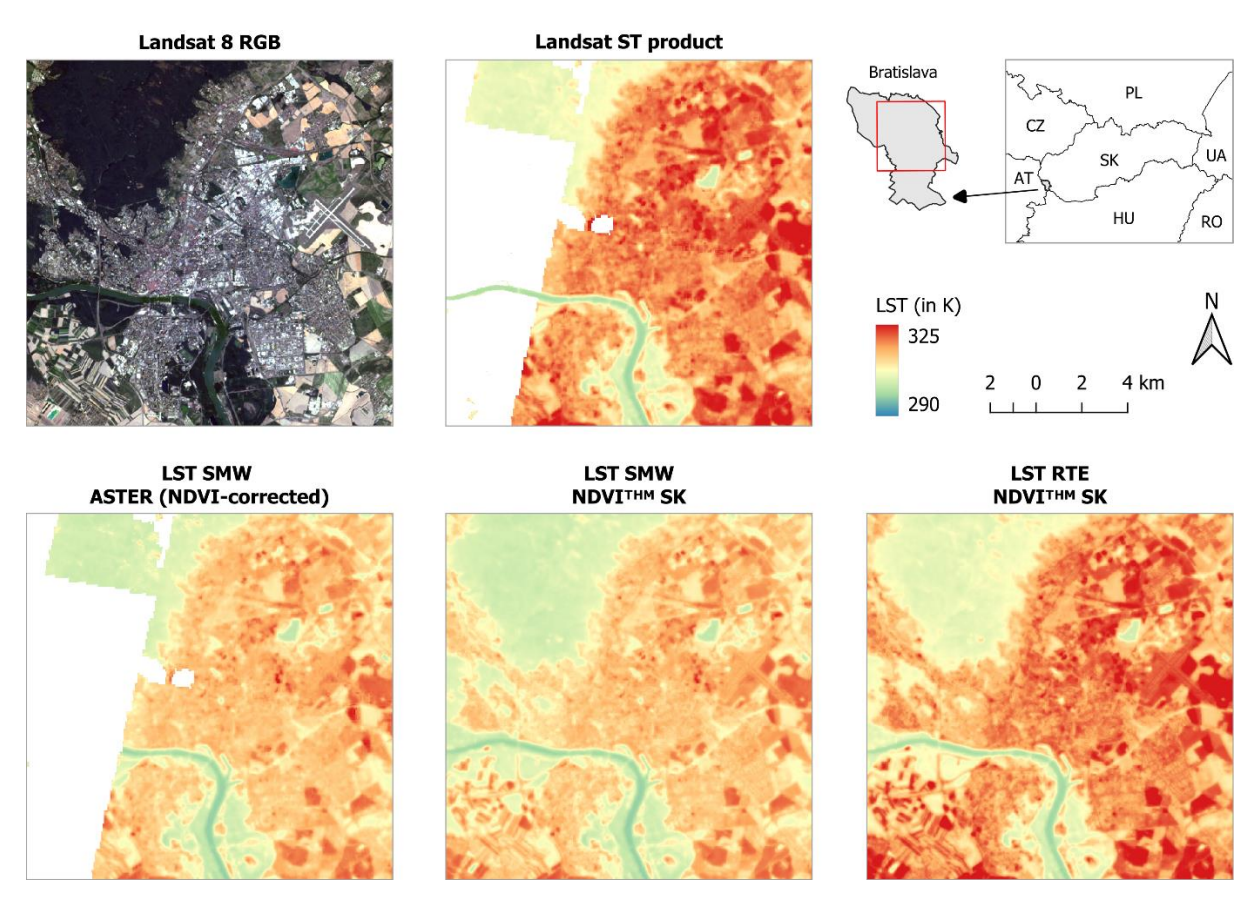


Fig. 2. Selected LST maps calculated from the Landsat 8 image retrieved on 22 July 2022 over Bratislava (the capital of the Slovak Republic).

Emissivity source comparisons revealed that NDVI-based methods improved performance over ASTER GEDv3 (NDVI-corrected). NDVI-based emissivity results in a more detailed spatial distribution of LST in heterogeneous urban areas, and produces LST maps free of block artifacts (Fig. 4). Except for SNDVI^{THM} WA, all NDVI-based SMW methods yielded lower RMSE than ASTER-based SMW (Table 3). Generally, the NDVI^{THM} proved to be more precise than the SNDVI^{THM} for both the SMW and RTE. For SMW, NDVI^{THM} SO produced the lowest RMSE (2.33 K) and the highest precision (1.31 K), but its discontinuities in emissivity at the NDVI threshold for bare soil (0.2) are followed by the discontinuities in LST. The same applies for the NDVI^{THM} YU method (Fig. S2) since the *C_i* component increases the emissivity of the mixed surfaces. The NDVI^{THM} SK method does not produce discontinuities, and was also evaluated as the most accurate emissivity model in the sensitivity analysis conducted by (Sekertekin and Bonafoni, 2020b). From SNDVI^{THM} methods, SNDVI^{THM} SK minimised the RMSE for both SMW and RTE. Consequently, we selected NDVI^{THM} SK and SNDVI^{THM} SK for further validation due to their robustness and smooth transitions across land cover types.

Table 3. RMSE (in K) for the Landsat 8 LST over the SURFRAD stations. Statistics for the original data (including outliers) are shown in grey, the lowest values are highlighted with a grey background. NDVI-based LSE was calculated with the vegetation threshold of 0.5.

Ctation	N	СТ	ST SMW		L	SE NDVITH	н	LS	SE SNDVIT	НМ
Station	14	31	LSE ASTER		SO	SK	YU	SK	YU	WA
	119	3.34	2.64	SMW	2.37	2.34	2.45	2.41	2.42	2.83
BND	123	4.10	3.45	SIVIVV	3.31	3.23	3.34	3.30	3.29	3.57
DND				RTE	3.17	3.19	3.35	3.25	3.28	3.82
				KIL	3.97	3.94	4.09	4.00	4.00	4.42
	149	2.74	2.13	SMW	2.17	2.09	2.00	2.18	2.06	2.04
DRA	160	8.31	7.70	SIVIVV	7.69	7.64	7.56	7.73	7.66	7.64
DKA				RTE	2.74	2.86	3.16	2.70	2.88	2.92
				KIE	8.28	8.28	8.33	8.30	8.33	8.33
	150	4.57	2.88	SMW	2.37	2.76	2.42	2.76	2.89	3.03
FPK	169	8.15	6.32	SIVIVV	6.03	6.23	6.03	6.26	6.32	6.39
FPK				RTE	3.79	4.45	3.92	4.32	4.46	4.62
				KIE	7.66	8.02	7.69	8.01	8.09	8.18
	169	1.71	1.57	CNAVA	1.69	1.56	1.66	1.56	1.54	1.68
GWN	175	2.39	2.25	SMW	2.39	2.25	2.36	2.25	2.23	2.30
GVVIN				RTE	1.68	1.63	1.72	1.69	1.71	2.09
				KIE	2.40	2.32	2.42	2.35	2.35	2.60
	37	2.62	2.37	SMW	2.32	2.25	2.31	2.53	2.54	2.92
PSU	39	6.26	5.67	SIVIVV	5.75	5.67	5.73	6.19	6.16	6.29
P30				RTE	2.51	2.50	2.60	2.55	2.56	2.95
				KIE	6.28	6.18	6.30	6.19	6.17	6.30
	106	2.97	2.42	SMW	2.19	2.22	2.27	2.31	2.60	2.67
SXF	111	3.97	3.43	SIVIVV	3.35	3.31	3.34	3.35	3.52	3.52
SAF				DTE	2.77	2.93	2.96	3.03	3.43	3.46
				RTE	3.85	3.90	3.93	3.95	4.22	4.22
	152	5.26	3.52	SMW	2.99	3.25	3.05	3.26	3.37	3.58
TBL	174	10.70	9.33	SIVIVV	9.19	9.23	9.17	9.26	9.28	9.34
IDL				DTE	4.16	4.58	4.21	4.70	4.83	5.06
				RTE	10.25	10.36	10.17	10.49	10.51	10.59
	882	3.61	2.58	SMW	2.33	2.42	2.33	2.46	2.50	2.70
All	951	7.15	6.18	SIVIVV	6.08	6.10	6.05	6.16	6.16	6.22
stations				DTE	3.13	3.40	3.28	3.39	3.49	3.75
				RTE	6.90	7.00	6.92	7.04	7.07	7.18

N – Number of validated Landsat 8 images

ST – USGS Landsat LST product

SMW – Statistical Mono-Window method (Ermida et al. 2008)

RTE - Radiative Transfer Equation method

ASTER – ASTER GEDv3 emissivity (NDVI-corrected)

NDVI^{THM} - NDVI threshold method

 $SNDVI^{THM}$ – Simplified NDVI threshold method

SK - Skoković et al. (2014)

YU - Yu et al. (2014)

WA – Wang et al. (2015)

SO - Sobrino et al. (2008)

The LST accuracy varied significantly by the SURFRAD station, reflecting the heterogeneity of the land surface. The lowest RMSE values were observed at GWN (1.57 K for SMW with ASTER), a uniform grassland site, while TBL (3.52 K) and FPK (2.88 K) exhibited the highest errors, likely due to complex terrain and mixed vegetation. These stations also showed elevated biases (up to 2.5 K), which persist even after removal of outliers, suggesting challenges in capturing LST over rugged or transitional landscapes. This spatial variability underscores the influence of surface characteristics on retrieval accuracy. Despite variable accuracy, SMW in conjunction with the NDVI-based emissivity proved to be the best method at all stations in terms of RMSE and precision.



377

378

373

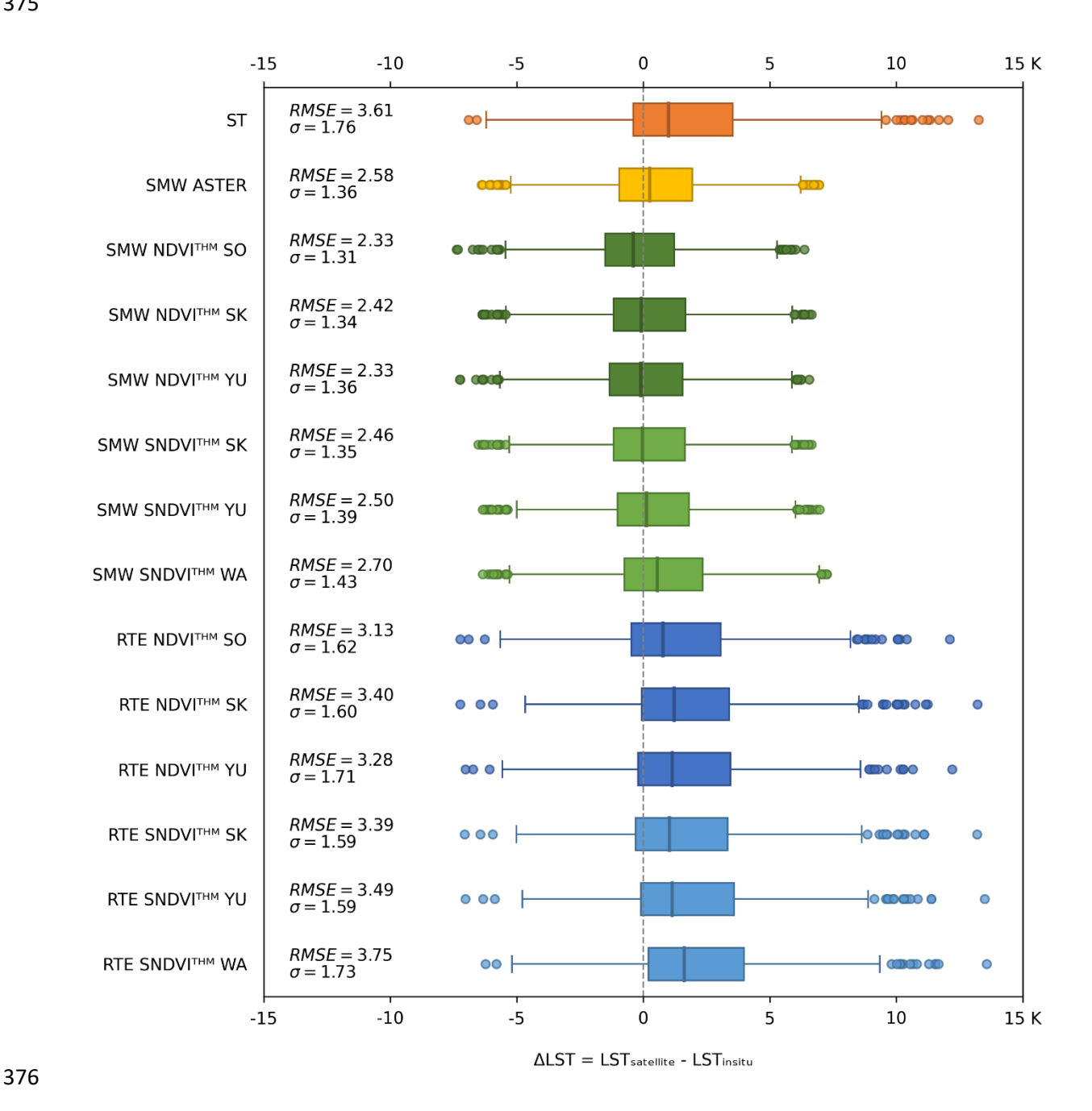


Fig. 3. Boxplots of differences between satellite-derived LST and in situ LST on a set of measurements from the Landsat 8 satellite.

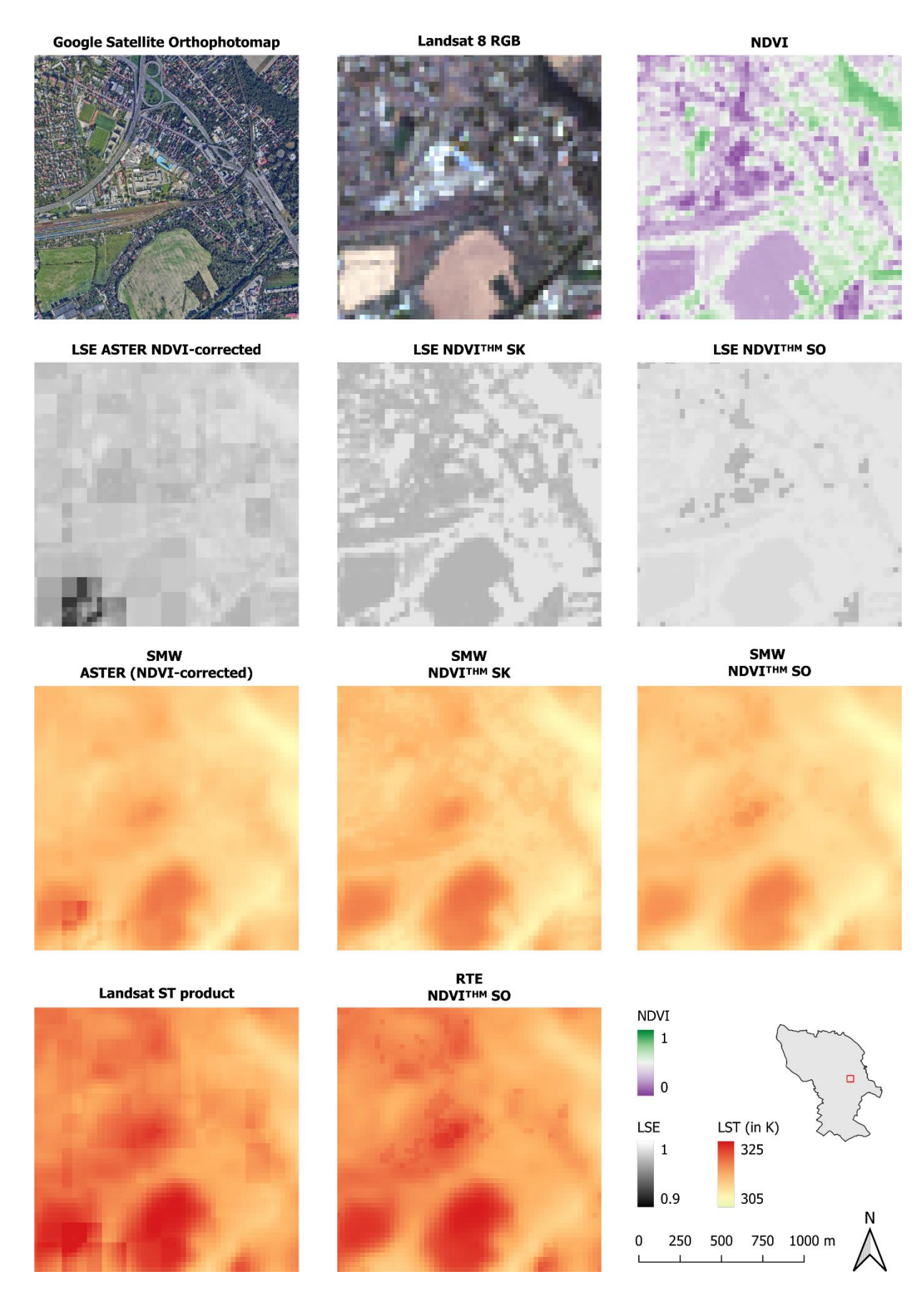


Fig. 4. Detailed section from selected land surface emissivity and LST maps derived from the Landsat 8 image retrieved on 22 July 2022 over Bratislava.

Extending validation to Landsat 5, 7, and 9 confirmed SMW's robustness across missions (Table 4, Table S2). Using NDVI^{THM} SK, SMW achieved RMSE values of 2.36 K (Landsat 5), 2.44 K (Landsat 7), 2.42 K (Landsat 8), and 2.62 K (Landsat 9), outperforming Landsat ST (3.47–3.92 K) and RTE (3.20–3.85 K). Landsat 8 displayed the highest accuracy (bias of -0.08 K), while Landsat 5 offered the best precision (1.31 K). However, differences in validation sets could influence the comparison of satellite missions. For example, Ermida et al. (2020) reported the highest accuracy for the Landsat 7 mission and the lowest RMSE for the Landsat 8 mission. Excluding high-bias stations (TBL and FPK) improved precision to approximately 1.1 K across missions, aligning with the 1K-threshold recommended for climate applications (Guillevic et al., 2018).

Table 4. Summary validation statistics for the Landsat 5, Landsat 7 and Landsat 9 LST at all SURFRAD stations: a - RMSE (in K), b - accuracy (μ , in K), c - precision (σ , in K). Statistics for the original data (including outliers) are shown in grey, the lowest values are highlighted with a grey background.

394 A

Mission	N	ST		SMW	RTE		
MISSIOII			ASTER	NDVITHM	SNDVITHM	NDVITHM	SNDVITHM
Landsat 5	1100	3.47	2.67	2.36	2.37	3.20	3.19
Lanusai 5	1148	4.56	3.88	3.66	3.70	4.31	4.35
Landsat 7	1563	3.58	2.68	2.44	2.49	3.20	3.20
Lanusat 1	1666	6.59	5.83	5.69	5.77	6.35	6.43
Landaat 0	882	3.61	2.58	2.42	2.46	3.40	3.39
Landsat 8	951	7.15	6.18	6.10	6.16	7.00	7.04
11 + 0	202	3.92	2.78	2.62	2.65	3.85	3.83
Landsat 9	212	5.33	4.33	4.23	4.27	5.28	5.29

Mississ	N	ST		SMW	RTE		
Mission			ASTER	NDVITHM	SNDVITHM	NDVITHM	SNDVITHM
Landoot E	1100	1.81	1.27	0.89	0.85	1.81	1.74
Landsat 5	1148	1.69	1.20	0.82	0.76	1.73	1.68
1 7	1563	1.46	0.70	0.41	0.37	1.32	1.18
Landsat 7	1666	1.29	0.62	0.29	0.26	1.20	1.08
Landoot 9	882	1.00	0.25	-0.08	-0.02	1.23	1.04
Landsat 8	951	0.89	0.17	-0.12	-0.07	1.11	0.85
Landsat 9	202	1.25	0.46	0.26	0.25	1.43	1.36
	212	1.19	0.45	0.22	0.20	1.38	1.34

396 C

Mission	N	ST		SMW	RTE		
WIISSION			ASTER	NDVITHM	SNDVITHM	NDVITHM	SNDVITHM
Landaat E	1100	1.81	1.43	1.31	1.37	1.50	1.60
Landsat 5	1148	1.95	1.51	1.41	1.49	1.57	1.66
Landsat 7	1563	1.85	1.52	1.39	1.45	1.59	1.65
Lanusat 1	1666	1.97	1.64	1.53	1.55	1.71	1.76
Landsat 8	882	1.76	1.36	1.34	1.35	1.60	1.59
Lanusaro	951	1.91	1.54	1.52	1.48	1.70	1.75
Landact O	202	1.72	1.49	1.44	1.51	1.68	1.65
Landsat 9	212	1.80	1.65	1.56	1.62	1.78	1.77

See Table 3 for explanations.

Our analysis establishes SMW, paired with NDVI^{THM} SK or SNDVI^{THM} SK, as the most accurate and precise method for LST retrieval across Landsat missions. It surpasses the Landsat ST product and RTE, particularly over homogeneous surfaces, though accuracy diminishes in complex terrains. These

results validate our GEE implementation as a reliable solution for LST mapping, overcoming limitations of ASTER GEDv3 and enhancing utility for environmental and climate studies.

5. Discussion

5.1. Comparison with previous LST studies

The best agreement with in-situ measurements was observed at BND, DRA, GWN, and SXF stations, while the largest deviations occurred at TBL and FPK stations. These findings are consistent with the validation results of Malakar et al. (2018), Ermida et al. (2020), and Cheng et al. (2021), except for DRA, where Malakar et al. (2018) and Cheng (2021) recorded higher deviations. However, following the Ermida et al. (2020) workflow, we obtained satellite LST from a point slightly north of that used in the Malakar et al. (2018) study, resulting in lower average LST and bias. TBL was also excluded from validation by Yu et al. (2014), Zhang et al. (2016), Sekertekin and Bonafoni (2020) and Duan et al. (2021). For the FPK station, Duan et al. (2021) reported the highest bias and RMSE in a similar way.

Several studies have compared the precision of various LST calculation methods. In Yu et al. (2014), the RTE method proved to be more accurate than the split-window (SW) and general single-channel (SC) method in the Landsat 8 validation set. Meanwhile, Sekertekin and Bonafoni (2020) showed that the mono-window (MW) algorithm yielded the highest accuracy for Landsat 7 and Landsat 8 missions, followed by the RTE method and then the SC method. García-Santos et al. (2018) also evaluated the RTE, SC and SW methods, although they used their own TIR broadband radiometer for validation instead of the SURFRAD stations. They found the SW method to be the most accurate, while the RTE had the highest RMSE but the lowest bias. However, these studies used limited validation sets, with only a few dozen satellite scenes, which could affect their results. As Cheng et al. (2021) note, comparing validation works under different conditions, such as varying quality control methods, parameter settings in LST calculation, or differing time periods in LST product/ground measurements, is unreasonable.

Our study's validation set comprised 1,100 Landsat 5 scenes, 1,563 Landsat 7 scenes, 882 Landsat 8 scenes, and 202 Landsat 9 scenes (after excluding outliers). This was made possible by the GEE data catalogue, eliminating the need to download large images. The same approach was employed by Ermida et al. (2020), and extensive validation of a new LST calculation method and the Landsat ST product was also carried out by Cheng et al. (2021). Our evaluation of Landsat ST products yielded bias/RMSE values of 1.81/3.47 K (Landsat 5), 1.46/3.58 K (Landsat 7), and 1.00/3.61 K (Landsat 8), aligned with the results of Cheng et al. (2021). Although Malakar et al. (2018) reported a higher accuracy for Landsat 5 and 7 products (RMSE 2.0–2.5 K), they used a limited set of four SURFRAD stations. After excluding FPK and TBL from the validation set, the RMSE values of 2.51 K (Landsat 5) and 2.50 K (Landsat 7) were closer to those reported by Malakar et al. (2018). These findings highlight the importance of carefully selecting the validation set.

Cheng et al. (2021) proposed a new method of LST calculation based on the RTE and separate emissivity calculations for different types of land surface. Although we did not directly compare this method with our approach, the RMSEs of the SMW method combined with NDVI^{THM} were lower across all Landsat missions (Table 4) than those reported by Cheng et al. (2021), which were 2.58 K, 3.21 K, and 2.95 K for Landsat 5, 7, and 8, respectively. This also applies to bias. However, Cheng et al. (2021) used a different validation set, including the BSRN and Huailai stations, so an exact comparison of the performance of the methods would require future analysis.

5.2. Influence of the NDVI on the emissivity and LST

445 Comparing the vegetation thresholds NDVI_V of 0.5 and 0.85 for the NDVI^{THM} emissivity calculation 446 showed slightly increased RMSEs of LST calculations with higher threshold at all stations (Fig. 5, Table 447 S3). Differences ranged up to 0.5 K, with a significantly smaller impact on the emissivity calculated by 448 the NDVI^{THM} SO and NDVI^{THM} YU method than the other NDVI-based methods. For example, at pixels

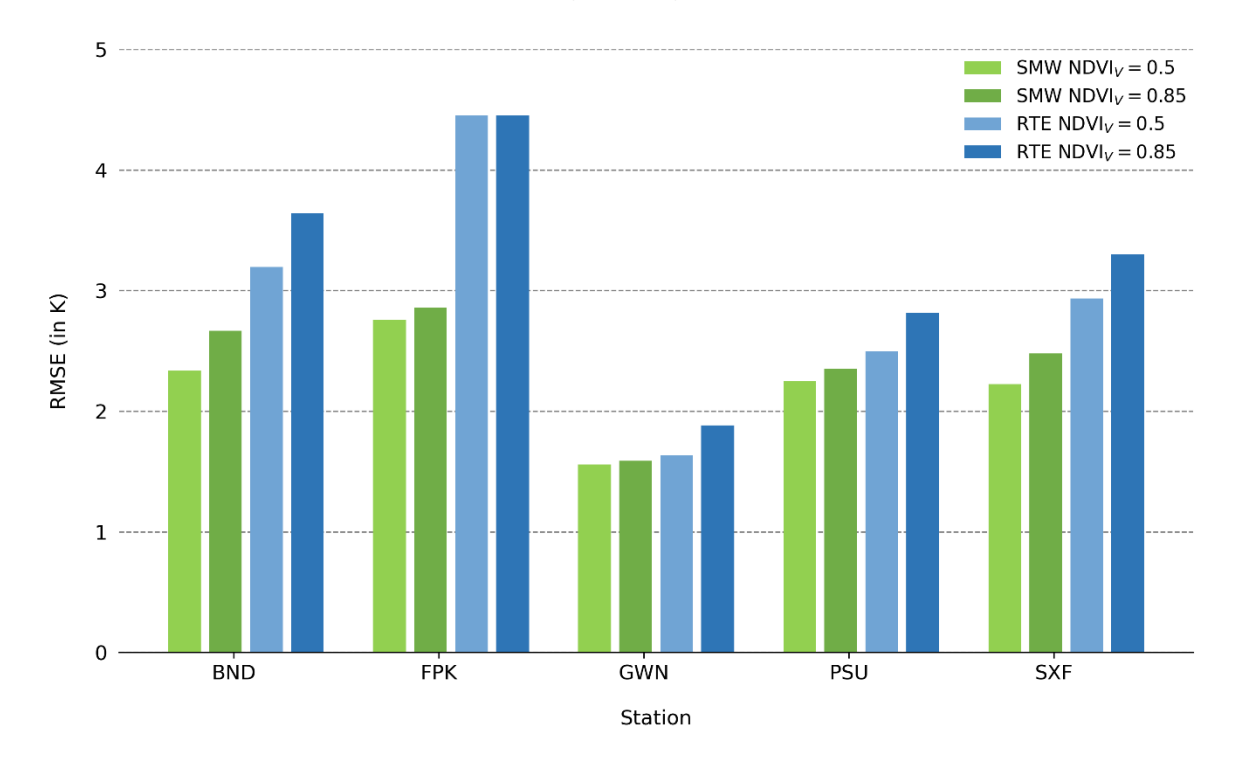


Fig. 5. Effect of a different threshold value of $NDVI_V$ on the accuracy of Landsat 8 LST retrieval by the statistical mono-window and radiative transfer equation methods (land surface emissivity was calculated by the $NDVI^{THM}$ SK method).

To better understand the relationship between satellite-derived LST accuracy and NDVI, we divided the Landsat 8 observations into three subsets: data points on bare soil (NDVI < 0.2), mixed surfaces ($0.2 \le NDVI \le 0.5$), and vegetated surfaces (NDVI > 0.5). Separate validations on these subsets revealed that the highest accuracy in the LST calculation was achieved on bare soil. Although soil emissivity values exhibit greater variability than vegetation emissivity values (Sobrino et al., 2004), LST values for bare soil had the smallest bias among all surface types (Fig. 6). At the same time, LST values on bare soil exhibited the highest range (from 240 K to over 330 K), while the lowest range was observed for values on vegetated surfaces. The highest RMSE errors and the lowest precision in LST calculations were recorded on mixed surfaces across all methods (Table S4). This suggests that mixed surfaces may be more sensitive to emissivity errors, which may not be accurately determined or corrected solely on the basis of NDVI. Valor and Caselles (1996) also found that emissivity can be calculated with a higher absolute error for mixed vegetation pixels (1-2%) compared to fully vegetated pixels (0.7-1%).

On mixed and vegetated surfaces, an overestimation of high LST values (above 300 K) can be observed, which is consistent with the findings of Ermida et al. (2020). The reduced precision of the LST calculation on surfaces at elevated temperatures was also predicted by the simulations of Jiménez-Muñoz and Sobrino (2006). The overestimation occured in all three validated methods, but is slightly more pronounced in the Landsat ST product and the RTE methods, especially on mixed surfaces (Fig. 6B). As a result, the RMSEs on mixed surfaces are significantly greater with the Landsat ST/RTE (3.55 to 4.29 K) than with the SMW methods (2.33 to 2.84 K). SMW, as an empirical algorithm, appears to better mitigate this overestimation bias, so we would recommend this method to be preferred in urban areas where most of the surface consists of mixed pixels.

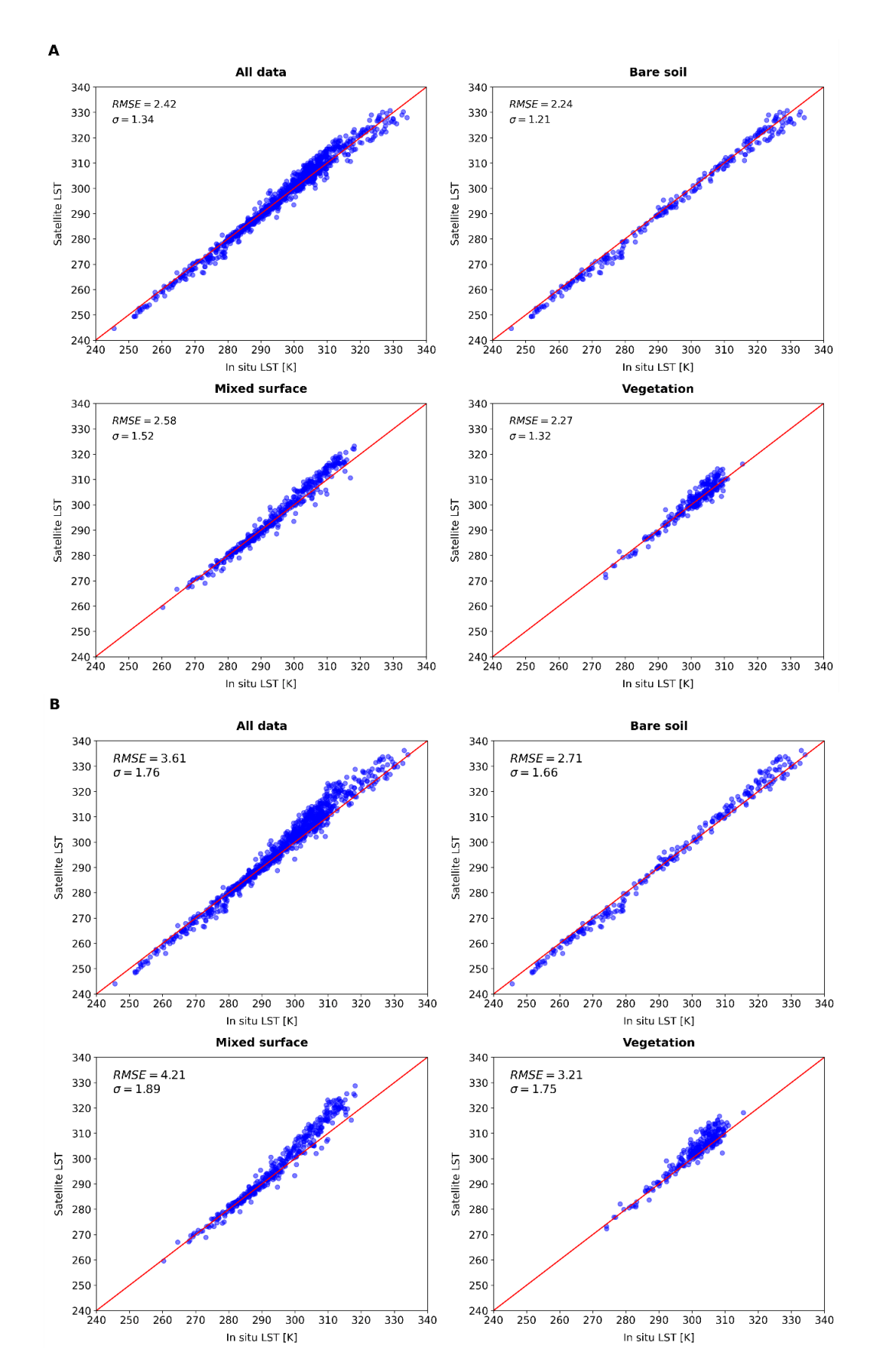


Fig. 6. Scatterplots of Landsat 8 LST against in-situ LST for subsets with different NDVI: bare soil (NDVI < 0.2), mixed surfaces (0.2 \leq NDVI \leq 0.5), and vegetated surfaces (NDVI > 0.5). A – statistical monowindow NDVI^{THM} SK method, B – Landsat ST product.

5.3. Limitations of the study

480

481 The results of our study have several limitations. The LST validation was conducted solely using in-situ 482 measurements from the SURFRAD network, whose stations are located in the USA. To improve the 483 robustness of the validation, the results need to be verified using measurements from other networks, 484 such as the BSRN (Baseline Surface Radiation Network), KIT (Karlsruhe Institute of Technology) network 485 or HiWATER. Furthermore, none of the SURFRAD stations are situated in urban areas, which limits our 486 ability to assess the accuracy of satellite-derived LST in heterogeneous urban environments, where 487 much of the surface consists of mixed pixels. The analysis dividing measurements based on NDVI 488 suggests that LST is likely determined most accurately in non-vegetated areas, where local surface heat 489 islands are most frequently formed.

490 Our research focused on two methods for calculating LST, namely radiative transfer equation and 491 statistical mono-window, which are the easiest to implement in the Google Earth Engine environment. 492 However, some studies suggest that other methods, such as MWA (Sekertekin and Bonafoni, 2020a) or SW (García-Santos et al., 2018), may be more accurate than RTE. It would also be important to 493 494 compare the precision of the RTE and SWM with the newly developed approach by Cheng et al. (2021). 495 However, implementing these methods in GEE would be more challenging, and an automatic 496 comparison across all cloud-free Landsat images would also be required. The testing of NDVI-based 497 methods could have been extended to include other published approaches, but this would significantly 498 increase the number of combinations tested. The same applies to evaluating multiple NDVI thresholds. 499 Ideally, the resulting emissivity layers would also be compared with in-situ land surface emissivity 500 measurements, as was done in the study by Cheng et al. (2021).

In future research, we plan to focus on comparing Landsat-based LST with more detailed sources of temperature data, such as aerial thermal cameras or microclimatic models. This comparison allows evaluating the spatial variability of different temperature sources and would help to assess the accuracy of detecting local urban heat islands from Landsat thermal images.

6. Conclusions

505

506

507

508

509

510

511

512

513

Although high-resolution geospatial data sources are increasingly available, detailed thermal imagery is still not widely used. Landsat satellite missions provide thermal imagery dating back to the 1980s at 30-meter resolution, currently available in the Google Earth Engine (GEE) global data catalog. The combination with the computational capabilities of this cloud platform offers rich possibilities for analyzing temperature changes in the era of global warming. Methods for obtaining land surface temperature (LST) from Landsat products have been developing for several decades, however, there are still weak points in their application. One source of uncertainty is the land surface emissivity data that enters the LST calculation and critically affects its accuracy.

- Our study implements the NDVI-based emissivity calculation in GEE, addressing the problem of missing data and block artifacts in the ASTER GEDv3 product, commonly used as the emissivity source for the LST calculation. While ASTER GEDv3 is a static product, NDVI-based emissivity allows for adaptation to spatio-temporal changes in vegetation, and also results in a more detailed spatial distribution of LST. In urban environments with high surface heterogeneity and frequent construction, NDVI-based LST calculation appears to be a more appropriate approach.
- The GEE code, combining NDVI-based emissivity with the statistical mono-window method by Ermida et al. (2020) and the radiative transfer equation method for Landsat LST calculation, is publicly available in the repository:
- 523 https://code.earthengine.google.com/?accept repo=users/hanabobalova/LST Landsat
- Validation against in-situ measurements from the SURFRAD network showed that statistical mono-
- 525 window method with the NDVI-based emissivity produces the most accurate results, while the

- 526 Landsat ST product and the RTE method overestimate LST at high temperatures, especially on mixed
- 527 surfaces. These results confirmed our GEE implementation as a reliable solution for LST mapping and
- 528 enhancing utility for urban climate studies.

References

- Arsad, F.S., Hod, R., Ahmad, N., Ismail, R., Mohamed, N., Baharom, M., Osman, Y., Radi, M.F.M.,
- Tangang, F., 2022. The Impact of Heatwaves on Mortality and Morbidity and the Associated
- Vulnerability Factors: A Systematic Review. Int. J. Environ. Res. Public Health 19.
- 533 https://doi.org/10.3390/ijerph192316356
- Augustine, J.A., DeLuisi, J.J., Long, C.N., 2000. SURFRAD A national surface radiation budget network
- for atmospheric research. Bull. Am. Meteorol. Soc. 81, 2341–2357.
- 536 https://doi.org/10.1175/1520-0477(2000)081<2341:SANSRB>2.3.CO;2
- Barsi, J.A., Barker, J.L., Schott, J.R., 2003. An Atmospheric Correction Parameter Calculator for a single
- thermal band earth-sensing instrument. IEEE Int. Geosci. Remote Sens. Symp. 2003 00, 2–4.
- 539 https://doi.org/10.1109/IGARSS.2003.1294665
- Becker, F., Li, Z.-L., 1990. Temperature-independent spectral indices in thermal infrared bands.
- 541 Remote Sens. Environ. 32, 17–33. https://doi.org/https://doi.org/10.1016/0034-
- 542 4257(90)90095-4
- 543 Carlson, T.N., Ripley, D.A., 1997. On the relation between NDVI, fractional vegetation cover, and leaf
- area index. Remote Sens. Environ. 62, 241–252. https://doi.org/10.1016/S0034-4257(97)00104-
- 545 1
- 546 Cheng, J., Meng, X., Dong, S., Liang, S., 2021. Generating the 30-m land surface temperature product
- over continental China and USA from landsat 5/7/8 data. Sci. Remote Sens. 4, 100032.
- 548 https://doi.org/10.1016/j.srs.2021.100032
- Cook, M., Schott, J.R., Mandel, J., Raqueno, N., 2014. Development of an Operational Calibration
- 550 Methodology for the Landsat Thermal Data Archive and Initial Testing of the Atmospheric
- 551 Compensation Component of a Land Surface Temperature (LST) Product from the Archive.
- 553 Crawford, C.J., Roy, D.P., Arab, S., Barnes, C., Vermote, E., Hulley, G., Gerace, A., Choate, M.,
- Engebretson, C., Micijevic, E., Schmidt, G., Anderson, C., Anderson, M., Bouchard, M., Cook, B.,
- Dittmeier, R., Howard, D., Jenkerson, C., Kim, M., Kleyians, T., Maiersperger, T., Mueller, C.,
- Neigh, C., Owen, L., Page, B., Pahlevan, N., Rengarajan, R., Roger, J.C., Sayler, K., Scaramuzza, P.,
- 557 Skakun, S., Yan, L., Zhang, H.K., Zhu, Z., Zahn, S., 2023. The 50-year Landsat collection 2 archive.
- 558 Sci. Remote Sens. 8, 100103. https://doi.org/10.1016/j.srs.2023.100103
- Dash, P., Göttsche, F.-M., Olesen, F., Fischer, H., 2001. Retrieval of land surface temperature and
- 560 emissivity from satellite data: Physics, theoretical limitations and current methods. J. Indian
- 561 Soc. Remote Sens. 29, 23–30. https://doi.org/10.1007/BF02989910
- Davies, L., Gather, U., 1993. The identification of multiple outliers. J. Am. Stat. Assoc. 88, 782–792.
- 563 https://doi.org/10.1080/01621459.1993.10476339
- 564 Duan, S.B., Li, Z.L., Li, H., Göttsche, F.M., Wu, H., Zhao, W., Leng, P., Zhang, X., Coll, C., 2019.
- Validation of Collection 6 MODIS land surface temperature product using in situ measurements.
- 566 Remote Sens. Environ. 225, 16–29. https://doi.org/10.1016/j.rse.2019.02.020
- 567 Duan, S.-B., Li, Z.-L., Zhao, W., Wu, P., Huang, C., Han, X.-J., Gao, M., Leng, P., Shang, G., 2021.
- Validation of Landsat land surface temperature product in the conterminous United States

- using in situ measurements from SURFRAD, ARM, and NDBC sites. Int. J. Digit. Earth 14, 640–
 660. https://doi.org/10.1080/17538947.2020.1862319
- 571 Duguay-Tetzlaff, A., Bento, V.A., Göttsche, F.M., Stöckli, R., Martins, J.P.A., Trigo, I., Olesen, F.,
- 572 Bojanowski, J.S., Da Camara, C., Kunz, H., 2015. Meteosat Land Surface Temperature Climate
- Data Record: Achievable Accuracy and Potential Uncertainties. Remote Sens. 7, 13139–13156.
- 574 https://doi.org/10.3390/rs71013139
- 575 Ermida, S.L., Soares, P., Mantas, V., Göttsche, F.M., Trigo, I.F., 2020. Google earth engine open-source 576 code for land surface temperature estimation from the landsat series. Remote Sens. 12, 1–21.
- 577 https://doi.org/10.3390/RS12091471
- García-Santos, V., Cuxart, J., Martínez-Villagrasa, D., Jiménez, M.A., Simó, G., 2018. Comparison of three methods for estimating land surface temperature from Landsat 8-TIRS Sensor data.
- 580 Remote Sens. 10, 1–13. https://doi.org/10.3390/rs10091450
- Gillespie, A., Rokugawa, S., Matsunaga, T., Cothern, J.S., Hook, S., Kahle, A.B., 1998. A temperature
 and emissivity separation algorithm for Advanced Spaceborne Thermal Emission and Reflection
 Radiometer (ASTER) images. IEEE Trans. Geosci. Remote Sens. 36, 1113–1126.
- Radiometer (ASTER) images. IEEE Trans. Geosci https://doi.org/10.1109/36.700995
- Gorelick, N., Hancher, M., Dixon, M., Ilyushchenko, S., Thau, D., Moore, R., 2017. Google Earth
 Engine: Planetary-scale geospatial analysis for everyone. Remote Sens. Environ. 202, 18–27.
 https://doi.org/10.1016/j.rse.2017.06.031
- Guillevic, P., Göttsche, F., Nickeson, J., Hulley, G., Ghent, D., Yu, Y., Trigo, I., Hook, S., Sobrino, J.A.,
 Remedios, J., Román, M., Camacho, F., 2018. Land Surface Temperature Product Validation Best
 Practice Protocol, in: Guillevic, P., Göttsche, F., Nickeson, J., Román, M. (Eds.), Good Practices
 for Satellite-Derived Land Product Validation. Land Product Validation Subgroup (WGCV/CEOS),
- 592 p. 58. https://doi.org/10.5067/doc/ceoswgcv/lpv/lst.001
- Hulley, G.C., Hook, S.J., Abbott, E., Malakar, N., Islam, T., Abrams, M., 2015. The ASTER Global
 Emissivity Dataset (ASTER GED): Mapping Earth's emissivity at 100 meter spatial scale. Geophys.
 Res. Lett. 42, 7966–7976. https://doi.org/10.1002/2015GL065564
- 596 IPCC (Intergovernmental Panel on Climate Change), 2021. Climate Change 2021: The Physical Science 597 Basis, the Working Group I contribution to the Sixth Assessment Report. Cambridge, UK.
- Jiménez-Muñoz, J.C., Sobrino, J.A., 2006. Error sources on the land surface temperature retrieved
 from thermal infrared single channel remote sensing data. Int. J. Remote Sens. 27, 999–1014.
 https://doi.org/10.1080/01431160500075907
- Jiménez-Muñoz, J.C., Cristóbal, J., Sobrino, J.A., Sòria, G., Ninyerola, M., Pons, X., 2009. Revision of the Single-Channel Algorithm for Land Surface Temperature Retrieval From Landsat Thermal-Infrared Data. IEEE Trans. Geosci. Remote Sens. 47, 339–349.
- 604 https://doi.org/10.1109/TGRS.2008.2007125
- Jiménez-Muñoz, J.C., Sobrino, J.A., Skoković, D., Mattar, C., Cristóbal, J., 2014. Land surface
 temperature retrieval methods from Landsat-8 thermal infrared sensor data. Geosci. Remote
 Sens. Lett. IEEE 11, 1840–1843. https://doi.org/10.1109/LGRS.2014.2312032
- Li, Z.L., Tang, B.H., Wu, H., Ren, H., Yan, G., Wan, Z., Trigo, I.F., Sobrino, J.A., 2013a. Satellite-derived
 land surface temperature: Current status and perspectives. Remote Sens. Environ. 131, 14–37.
 https://doi.org/10.1016/j.rse.2012.12.008
- 611 Li, Z.L., Wu, H., Wang, N., Qiu, S., Sobrino, J.A., Wan, Z., Tang, B.H., Yan, G., 2013b. Land surface 612 emissivity retrieval from satellite data. Int. J. Remote Sens. 34, 3084–3127.

- 613 https://doi.org/10.1080/01431161.2012.716540
- 614 Li, Z.L., Wu, H., Duan, S.B., Zhao, W., Ren, H., Liu, X., Leng, P., Tang, R., Ye, X., Zhu, J., Sun, Y., Si, M.,
- Liu, M., Li, J., Zhang, X., Shang, G., Tang, B.H., Yan, G., Zhou, C., 2023. Satellite Remote Sensing
- of Global Land Surface Temperature: Definition, Methods, Products, and Applications. Rev.
- 617 Geophys. 61, 1–77. https://doi.org/10.1029/2022RG000777
- 618 Liu, Y., Yu, Y., Yu, P., Göttsche, F.M., Trigo, I.F., 2015. Quality assessment of S-NPP VIIRS land surface 619 temperature product. Remote Sens. 7, 12215–12241. https://doi.org/10.3390/rs70912215
- Liu, Y., Yu, P., Wang, H., Peng, J., Yu, Y., 2022. Ten Years of VIIRS Land Surface Temperature Product Validation. Remote Sens. 14. https://doi.org/10.3390/rs14122863
- Malakar, N.K., Hulley, G.C., Hook, S.J., Laraby, K., Cook, M., Schott, J.R., 2018. An Operational Land
 Surface Temperature Product for Landsat Thermal Data: Methodology and Validation. IEEE
 Trans. Geosci. Remote Sens. 56, 5717–5735. https://doi.org/10.1109/TGRS.2018.2824828
- 625 Martin, M.A., Ghent, D., Pires, A.C., Göttsche, F.M., Cermak, J., Remedios, J.J., 2019. Comprehensive 626 in situ validation of five satellite land surface temperature data sets over multiple stations and 627 years. Remote Sens. 11. https://doi.org/10.3390/rs11050479
- Mohamed, A.A., Odindi, J., Mutanga, O., 2016. Land Surface Temperature and Emissivity Estimation for Urban Heat Island assessment using medium and low resolution space-borne sensors: A review. Geocarto Int. 6049, 1–41. https://doi.org/10.1080/10106049.2016.1155657
- Ndossi, M.I., Avdan, U., 2016. Application of open source coding technologies in the production of Land Surface Temperature (LST) maps from Landsat: A PyQGIS plugin. Remote Sens. 8. https://doi.org/10.3390/rs8050413
- Parastatidis, D., Mitraka, Z., Chrysoulakis, N., Abrams, M., 2017. Online global land surface temperature estimation from landsat. Remote Sens. 9, 1–16. https://doi.org/10.3390/rs9121208
- Qin, Z., Karnieli, A., Berliner, P., 2001. A mono-window algorithm for retrieving land surface
 temperature from Landsat TM data and its application to the Israel-Egypt border region. Int. J.
 Remote Sens. 22, 3719–3746. https://doi.org/10.1080/01431160010006971
- Ren, H., Liu, R., Qin, Q., Fan, W., Yu, L., Du, C., 2017. Mapping finer-resolution land surface emissivity using Landsat images in China. J. Geophys. Res. 122, 6764–6781. https://doi.org/10.1002/2017JD026910
- Sekertekin, A., Bonafoni, S., 2020a. Land surface temperature retrieval from Landsat 5, 7, and 8 over rural areas: Assessment of different retrieval algorithms and emissivity models and toolbox implementation. Remote Sens. 12. https://doi.org/10.3390/rs12020294
- Sekertekin, A., Bonafoni, S., 2020b. Sensitivity analysis and validation of daytime and nighttime land surface temperature retrievals from landsat 8 using different algorithms and emissivity models. Remote Sens. 12. https://doi.org/10.3390/RS12172776
- Snyder, W.C., Wan, Z., Zhang, Y., Feng, Y.-Z., 1998. Classification-based emissivity for land surface
 temperature measurement from space. Int. J. Remote Sens. 19, 2753–2774.
 https://doi.org/10.1080/014311698214497
- Sobrino, J.A., Jiménez-Muñoz, J.C., Paolini, L., 2004. Land surface temperature retrieval from
 LANDSAT TM 5. Remote Sens. Environ. 90, 434–440. https://doi.org/10.1016/j.rse.2004.02.003
- Sobrino, J.A., Jiménez-Muñoz, J.C., Sòria, G., Romaguera, M., Guanter, L., Moreno, J., Plaza, A.,
 Martínez, P., 2008. Land surface emissivity retrieval from different VNIR and TIR sensors. IEEE

656	Trans. Geosci. Remote Sens. 46, 316–327. https://doi.org/10.1109/TGRS.2007.904834
657 658 659	Sobrino, J.A., Raissouni, N., 2000. Toward remote sensing methods for land cover dynamic monitoring: Application to Morocco. Int. J. Remote Sens. 21, 353–366. https://doi.org/10.1080/014311600210876
660 661 662	Tang, BH., Shao, K., Li, ZL., Wu, H., Tang, R., 2015. An improved NDVI-based threshold method for estimating land surface emissivity using MODIS satellite data. Int. J. Remote Sens. 36, 4864–4878. https://doi.org/10.1080/01431161.2015.1040132
663 664	UN (United Nations), 2019. World Urbanization Prospects: The 2018 Revision. United Nations, Department of Economic and Social Affairs, Population Division, New York.
665 666	USGS (U.S.Geological Survey), 2021. Landsat 8-9 Calibration and Validation (Cal/Val) Algorithm Description Document (ADD) Version 4., 807.
667 668	USGS (U.S.Geological Survey), n.d. Landsat Collection 2 Surface Temperature [WWW Document]. URL https://www.usgs.gov/landsat-missions/landsat-collection-2-surface-temperature
669 670 671	Valor, E., Caselles, V., 1996. Mapping land surface emissivity from NDVI: Application to European, African, and South American areas. Remote Sens. Environ. 57, 167–184. https://doi.org/https://doi.org/10.1016/0034-4257(96)00039-9
672 673 674	van de Griend, A.A., Owe, M., 1993. On the relationship between thermal emissivity and the normalized difference vegetation index for natural surfaces. Int. J. Remote Sens. 14, 1119–1131. https://doi.org/10.1080/01431169308904400
675 676	Voogt, J. a., Oke, T.R., 2003. Thermal remote sensing of urban climates. Remote Sens. Environ. 86, 370–384. https://doi.org/10.1016/S0034-4257(03)00079-8
677 678 679	Wang, K., Liang, S., 2009. Evaluation of ASTER and MODIS land surface temperature and emissivity products using long-term surface longwave radiation observations at SURFRAD sites. Remote Sens. Environ. 113, 1556–1565. https://doi.org/10.1016/j.rse.2009.03.009
680 681 682	Yu, X., Guo, X., Wu, Z., 2014. Land surface temperature retrieval from landsat 8 TIRS-comparison between radiative transfer equation-based method, split window algorithm and single channel method. Remote Sens. 6, 9829–9852. https://doi.org/10.3390/rs6109829
683 684 685	Zhang, Z., He, G., Wang, M., Long, T., Wang, G., Zhang, X., 2016. Validation of the generalized single-channel algorithm using landsat 8 imagery and SURFRAD ground measurements. Remote Sens. Lett. 7, 810–816. https://doi.org/10.1080/2150704X.2016.1190475
686	
687	
688	
689	
690	
691	
692	
693	
601	

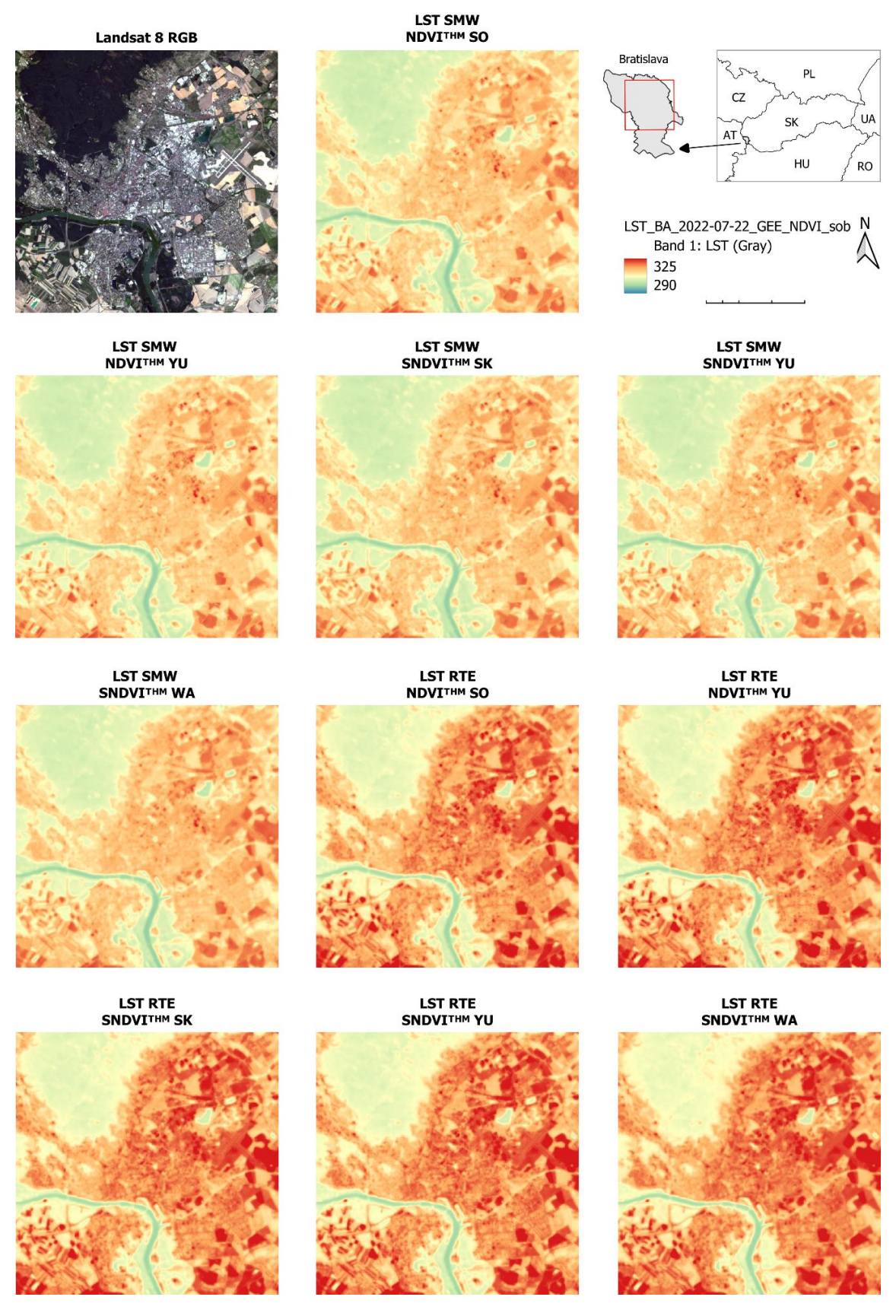


Fig. S1. Selected LST maps calculated by the RTE and SMW methods from the Landsat 8 image retrieved on 22 July 2022 over Bratislava.

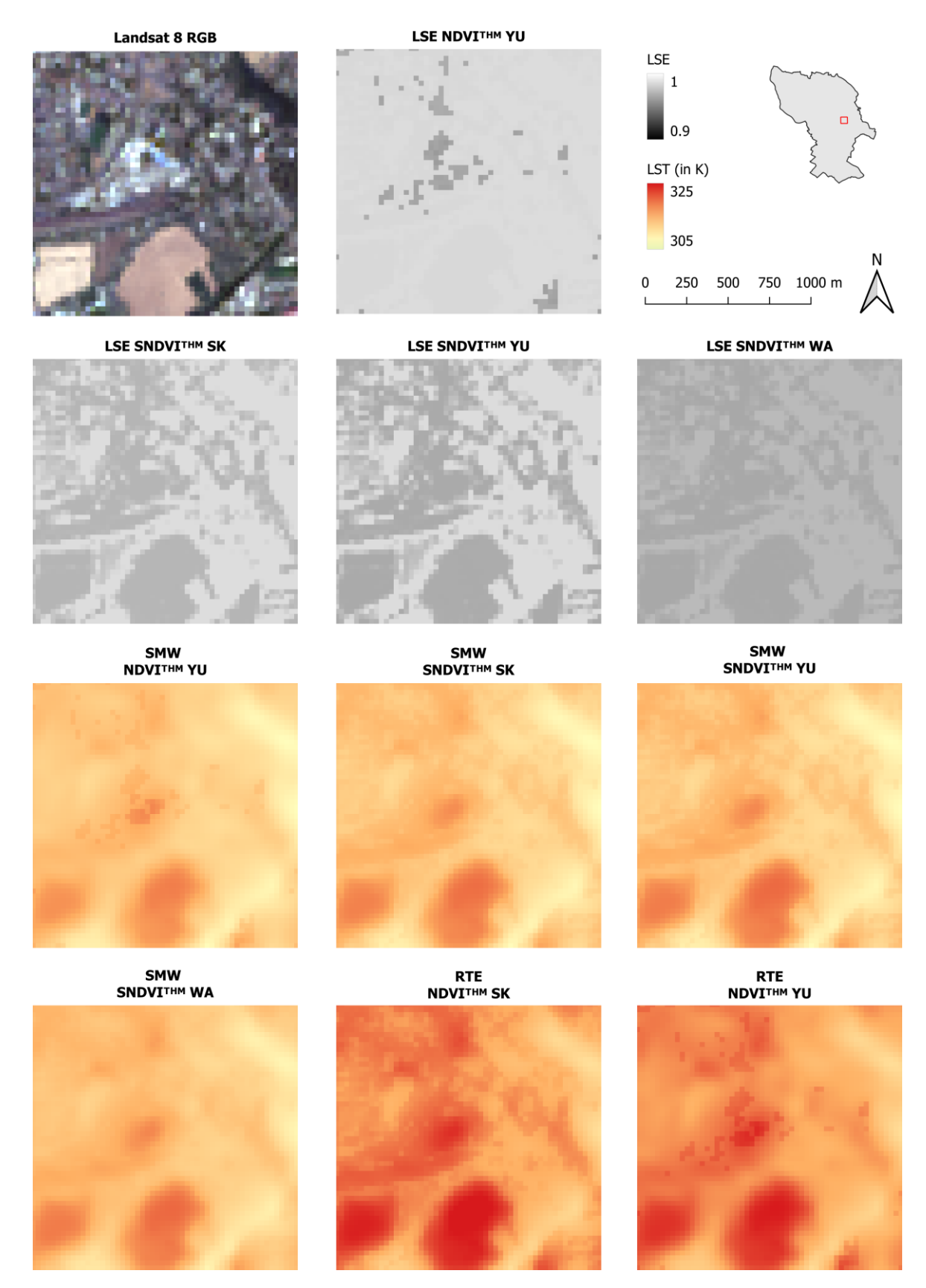


Figure S2: Cont.

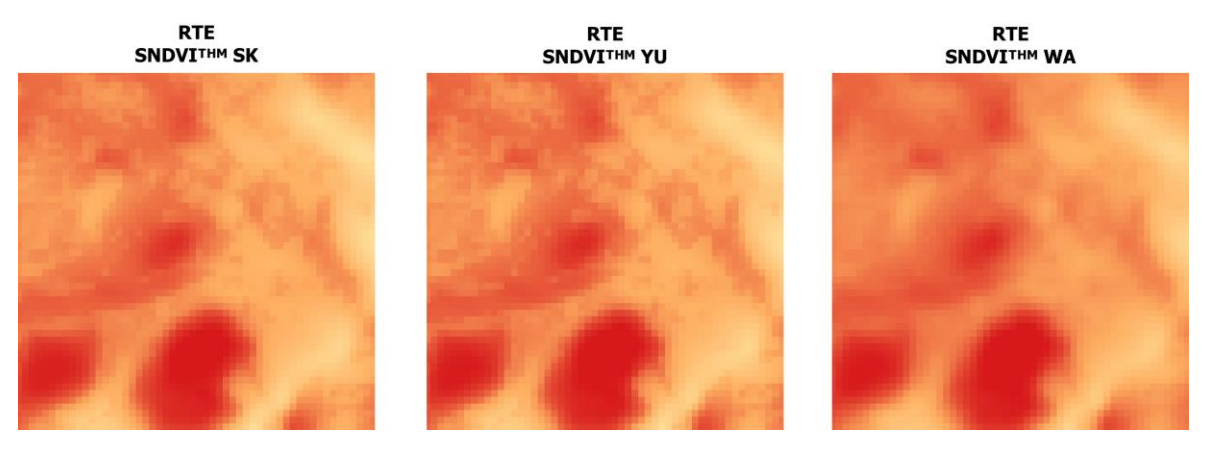


Fig. S2. Detailed section from selected LSE and LST maps derived from the Landsat 8 image retrieved on 22 July 2022 over Bratislava.

Table S1. Accuracy and precision for the Landsat 8 LST over the SURFRAD stations, with LSE calculated using the vegetation threshold NDVI_V = 0.5: a– accuracy/bias (μ , in K), b– precision (σ , in K). Statistics for the original data (including outliers) are shown in grey, the lowest values are highlighted with a grey background.

710 A

Ctation	A.I	СТ	SMW		L	SE NDVITI	НМ	LS	SE SNDVIT	НМ
Station	N	ST	LSE ASTER		SO	SK	YU	SK	YU	WA
	119	1.22	0.83	SMW	0.19	0.29	0.38	0.43	0.51	1.12
DND	123	1.10	0.68	SIVIVV	0.08	0.23	0.30	0.39	0.44	1.07
BND				RTE	1.22	1.39	1.44	1.32	1.44	2.08
				KIE	1.15	1.33	1.35	1.24	1.36	1.99
	149	1.17	-0.59	CNAVA/	-0.64	-0.46	0.04	-0.74	-0.32	-0.25
DDA	160	0.79	-0.76	SMW	-0.87	-0.63	-0.07	-0.89	-0.55	-0.49
DRA				DTE	0.97	1.18	1.65	1.10	1.41	1.46
				RTE	0.75	0.92	1.34	0.72	1.03	1.08
	150	1.96	0.93	CNAVA	-0.08	0.68	0.01	0.68	0.83	1.09
FPK	169	2.20	1.06	SMW	0.14	0.84	0.26	0.84	0.99	1.25
FPK				DTE	1.55	2.33	1.76	1.77	2.02	2.19
				RTE	1.59	2.48	1.89	1.92	2.13	2.42
	169	0.30	0.10	CN 4VA/	-0.66	-0.27	-0.50	-0.17	-0.04	0.47
OMA	175	0.27	0.08	SMW	-0.72	-0.32	-0.52	-0.18	-0.10	0.43
GWN				DTE	0.00	0.31	0.15	0.41	0.55	1.14
			RTE	-0.04	0.29	0.14	0.40	0.50	1.12	
	37 0.38 -0.3	-0.31	CNAVA	-1.00	-0.71	-0.80	0.43	0.47	1.24	
DOLL	39	0.30	-0.44	SMW	-1.01	-0.77	-0.86	0.37	0.41	1.08
PSU				DTE	0.26	0.34	0.48	0.44	0.48	1.29
				RTE	0.24	0.26	0.47	0.43	0.47	1.08
	106	0.81	0.22	CNAVA	-0.46	0.01	-0.33	0.10	0.13	0.59
CVE	111	0.77	0.02	SMW	-0.59	-0.08	-0.43	-0.08	0.01	0.38
SXF				DTE	0.80	1.50	1.31	1.09	1.20	1.73
				RTE	0.77	1.42	1.17	0.86	1.00	1.57
	152	2.74	1.33	CN 4VA/	0.02	1.07	0.34	1.07	1.42	1.51
TDI	174	2.27	1.02	SMW	-0.14	0.67	0.00	0.67	0.91	1.14
TBL				DTE	1.54	2.27	1.62	2.35	2.63	2.68
				RTE	0.95	1.78	1.10	1.78	2.01	2.22
	882	1.00	0.25	CNAVA	-0.40	-0.08	-0.10	-0.02	0.12	0.56
All	951	0.89	0.17	SMW	-0.47	-0.12	-0.19	-0.07	0.12	0.54
stations				DTE	0.77	1.23	1.14	1.04	1.15	1.63
				RTE	0.71	1.11	1.07	0.85	1.03	1.52

721 B

ь			01011			SE NDVIT	нм	1.0	SE SNDVIT	нм
Station	N	ST	SMW LSE ASTER	-	SO	SK	YU	SK	YU YU	WA
	119	1.70				-	1.28	1.19	1.16	1.37
		1.70	1.30	SMW	1.26 1.28	1.15 1.17	1.20	1.19	1.10	1.37
BND	123	1.01	1.24		1.60		1.66		1.46	
				RTE		1.44		1.50		1.63
	110	4 47	4.07		1.57	1.54	1.72	1.48	1.48	1.59
	149	1.47	1.27	SMW	1.29	1.30	1.28	1.24	1.27	1.28
DRA	160	1.52	1.43		1.42	1.46	1.48	1.41	1.42	1.41
				RTE	1.46	1.46	1.46	1.47	1.48	1.49
					1.55	1.57	1.61	1.53	1.54	1.54
	150	3.06	2.37	SMW	1.64	2.02	1.72	2.02	2.06	2.19
FPK	169	3.37	2.85	CIVIVV	1.98	2.28	2.08	2.28	2.43	2.50
				RTE	2.06	2.19	1.89	2.48	2.52	2.57
				KIL	2.51	2.60	2.29	2.83	2.80	2.99
	169	0.89	0.86	SMW	0.87	0.84	0.90	0.87	0.87	0.81
GWN	175	0.91	0.89		0.93	0.87	0.95	0.94	0.90	0.88
GWN				DTE	0.96	0.93	0.98	0.91	0.92	0.93
			RTE	0.99	0.96	1.03	0.93	0.96	0.96	
	37	1.38	0.83	ON 4147	0.86	0.98	0.90	1.25	1.25	1.30
2011	39	1.45	0.92	SMW	0.91	0.99	0.95	1.37	1.31	1.41
PSU					1.23	1.34	1.42	1.42	1.28	1.44
				RTE	1.42	1.41	1.43	1.43	1.38	1.44
	106	1.56	1.37		1.06	1.29	1.13	1.36	1.36	1.48
	111	1.66	1.41	SMW	1.15	1.33	1.23	1.33	1.29	1.57
SXF					1.45	1.45	1.50	1.57	1.48	1.73
				RTE	1.50	1.44	1.46	1.62	1.54	1.80
	152	3.21	2.38		2.23	2.25	2.20	2.25	2.27	2.35
	174	3.95	2.74	SMW	2.47	2.69	2.50	2.69	2.75	2.75
TBL					2.87	2.87	2.61	2.96	2.94	3.14
				RTE	3.12	3.21	2.93	3.57	3.56	3.72
	882	1.76	1.36		1.31	1.34	1.36	1.35	1.39	1.43
All	951	1.91	1.54	SMW	1.42	1.52	1.48	1.48	1.51	1.60
stations	301	1.01	1.01		1.62	1.60	1.71	1.59	1.59	1.73
				RTE						1.85
				—	1.74	1.70	1.84	1.75	1.72	1.8

N – Number of validated Landsat 8 images

ST – USGS Landsat LST product

SMW – Statistical Mono-Window method (Ermida et al. 2008)

RTE – Radiative Transfer Equation method

 $NDVI^{THM}-NDVI \ threshold \ method$

 ${\sf SNDVI}^{\sf THM} - {\sf Simplified\ NDVI\ threshold\ method}$

SK - Skoković et al. (2014)

YU - Yu et al. (2014)

WA – Wang et al. (2015)

SO - Sobrino et al. (2008)

722

723

724

729 A

Station	N	ST		SMW	RTE		
Station	74		ASTER	NDVITHM	SNDVITHM	NDVITHM	SNDVITHM
BND	182	2.78	2.70	2.37	2.44	2.80	2.87
БИО	188	3.87	3.44	3.17	3.26	3.75	3.91
DRA	172	2.93	1.78	1.80	1.65	3.01	2.76
DKA	175	3.16	2.22	2.24	2.16	3.22	3.02
FPK	195	3.85	2.85	2.68	2.68	3.70	3.72
FFK	206	5.03	4.07	3.91	3.96	4.84	4.91
GWN	219	1.98	2.19	1.98	2.01	2.01	2.04
GVVIV	226	3.27	3.33	3.19	3.22	3.23	3.27
PSU	50	2.10	2.09	1.96	2.26	2.25	2.26
F30	51	2.37	2.43	2.33	2.50	2.50	2.50
SXF	72	2.38	1.98	1.80	1.83	2.41	2.46
SAF	75	3.19	2.93	2.82	2.84	3.14	3.18
TDI	210	5.33	3.69	2.97	2.98	4.39	4.40
TBL	227	6.83	5.67	5.25	5.33	6.14	6.23

730 B

Ctation	A.	ST		SMW	RTE		
Station	N	31	ASTER	NDVITHM	SNDVITHM	NDVITHM	SNDVITHM
BND	202	3.06	2.56	2.26	2.33	2.90	2.93
рир	212	4.94	4.19	4.04	4.08	4.81	4.87
DRA	311	2.56	1.82	1.82	1.97	2.45	2.29
DKA	332	5.57	5.32	5.26	5.42	5.44	5.53
FPK	277	4.61	3.30	3.13	3.13	4.19	4.22
FFK	304	6.09	5.10	4.97	4.99	5.75	5.79
GWN	290	2.11	2.28	2.06	2.10	2.06	2.10
GWN	303	4.86	4.28	4.17	4.20	4.81	4.84
PSU	81	2.04	1.89	1.86	2.06	2.19	2.06
P30	86	3.73	3.49	3.38	3.67	3.59	3.67
SXF	159	2.42	2.19	2.04	2.08	2.30	2.32
SAF	163	4.70	4.31	4.22	4.26	4.54	4.59
TDI	243	5.62	3.67	3.12	3.13	4.59	4.62
TBL	266	11.26	9.86	9.63	9.73	10.77	10.92

731 C

				SMW	RTE		
Station	N	ST	ASTER	NDVITHM	SNDVITHM	NDVITHM	SNDVITHM
BND -	27	3.45	2.56	2.24	2.31	3.38	3.43
БИО -	28	3.78	2.92	2.70	2.75	3.74	3.77
DDA	35	3.43	2.95	2.91	2.97	3.57	3.46
DRA	36	3.49	3.17	3.13	3.20	3.61	3.51
EDV	31	5.07	2.95	2.85	2.90	5.23	5.08
FPK	37	8.84	6.98	6.85	6.94	8.83	8.84
CVA/NI	35	1.57	1.39	1.29	1.30	1.54	1.60
GWN	35	1.57	1.39	1.29	1.30	1.54	1.60
DCLI	12	2.19	2.06	2.23	2.18	2.14	2.14
PSU	12	2.19	2.06	2.23	2.18	2.14	2.14
CVE	23	2.52	2.21	1.98	2.04	2.47	2.52
SXF	24	2.74	2.63	2.44	2.48	2.63	2.68
TDI	39	5.25	3.56	3.28	3.28	4.80	4.87
TBL	40	7.02	5.67	5.57	5.56	6.80	6.84

Table S3. Validation statistics for the Landsat 8 LST over the SURFRAD stations, with LSE calculated using the vegetation threshold NDVI_V = 0.85: a – RMSE (in K), b – accuracy (μ , in K), c – precision (σ , in K). Statistics for the original data (including outliers) are shown in grey, the lowest values are highlighted with a grey background.

735 A

Station	N	ST	SMW LSE ASTER		LSE NDVITHM			LSE SNDVITHM			
				•	SO	SK	YU	SK	YU	WA	
BND	119	3.34	2.64	CN 41A7	2.42	2.67	2.47	2.66	2.75	2.97	
	123	4.10	3.45	SMW	3.34	3.45	3.35	3.47	3.52	3.67	
				DTC	3.25	3.64	3.38	3.60	3.71	3.99	
				RTE	4.03	4.28	4.11	4.26	4.34	4.55	
	150	4.57	2.88	CNAVA	2.39	2.86	2.42	2.86	3.02	3.08	
EDV	169	8.15	6.32	SMW	6.03	6.27	6.03	6.30	6.38	6.41	
FPK				RTE	3.82	4.45	3.93	4.43	4.61	4.67	
					7.68	8.02	7.69	8.07	8.17	8.21	
	169	1.71	1.57	SMW	1.67	1.59	1.66	1.59	1.62	1.76	
CVA/NI	175	2.39	2.25		2.37	2.26	2.36	2.26	2.26	2.35	
GWN				DTC	1.70	1.88	1.74	1.88	1.98	2.22	
				RTE	2.41	2.47	2.42	2.47	2.52	2.69	
	37	2.62	2.37	SMW	2.32	2.35	2.32	2.77	2.86	3.07	
DCII	39	6.26	5.67		5.74	5.68	5.73	6.26	6.27	6.34	
PSU				DTE	2.56	2.81	2.62	2.80	2.89	3.10	
				RTE	6.29	6.28	6.30	6.27	6.28	6.35	
	106	2.97	2.42	SMW	2.23	2.48	2.26	2.48	2.58	2.72	
CVE	111	3.97	3.43	SIVIVV	3.37	3.45	3.37	3.46	3.51	3.59	
SXF				DTE	2.84	3.30	2.95	3.27	3.40	3.57	
				RTE	3.89	4.14	3.95	4.13	4.21	4.32	

737 B

,											
Station	N	CT	SMW LSE ASTER		LSE NDVITHM			LSE SNDVITHM			
	/4	ST			SO	SK	YU	SK	YU	WA	
BND	119	1.22	0.83	CNAVA	0.29	0.82	0.43	0.82	0.97	1.28	
	123	1.10	0.68	SMW	0.19	0.74	0.34	0.74	0.86	1.26	
				RTE	1.31	2.02	1.49	1.70	1.91	2.26	
				KIE	1.26	1.88	1.40	1.64	1.81	2.07	
	150	1.96	0.93	CNAVA	-0.07	0.89	0.01	0.89	1.09	1.17	
EDV	169	2.20	1.06	SMW	0.20	1.00	0.30	1.00	1.30	1.37	
FPK				RTE	1.55	2.33	1.76	1.88	2.15	2.22	
					1.60	2.48	1.94	2.10	2.37	2.43	
GWN	169	0.30	0.10	CNAVA	-0.56	0.18	-0.43	0.18	0.40	0.61	
	175	0.27	0.08	SMW	-0.57	0.15	-0.46	0.15	0.37	0.60	
				RTE	0.07	0.81	0.18	0.81	1.03	1.31	
				KIE	0.06	0.74	0.18	0.74	0.94	1.28	
	37	0.38	-0.31	CNAVA	-0.89	-0.39	-0.78	0.66	0.89	1.29	
DCII	39	0.30	-0.44	SMW	-0.94	-0.46	-0.81	0.51	0.62	1.21	
PSU				DTC	0.26	0.68	0.48	0.66	0.89	1.29	
				RTE	0.24	0.66	0.47	0.51	0.62	1.21	
SXF	106	0.81	0.22	CNAVA	-0.39	0.34	-0.31	0.34	0.56	0.65	
	111	0.77	0.02	SMW	-0.50	0.15	-0.38	0.15	0.38	0.60	
				DTC	0.86	1.71	1.33	1.47	1.72	1.86	
				RTE	0.80	1.56	1.23	1.42	1.64	1.78	
					0.00	1.50	1.20	1.42	1.04	1.0	

Station	N	ST	SMW		LSE NDVITHM			LSE SNDVITHM			
			LSE ASTER	-	SO	SK	YU	SK	YU	WA	
	119	1.70	1.30	SMW	1.28	1.27	1.31	1.27	1.25	1.33	
DND	123	1.81	1.24		1.32	1.28	1.33	1.28	1.29	1.35	
BND				DTE	1.59	1.62	1.67	1.53	1.51	1.72	
				RTE -	1.64	1.68	1.72	1.52	1.52	1.64	
	150	3.06	2.37	SMW	1.65	2.08	1.72	2.08	2.20	2.20	
FPK	169	3.37	2.85	SIVIVV	2.03	2.39	2.11	2.39	2.43	2.43	
FFK				RTE -	2.01	2.19	1.89	2.56	2.57	2.58	
					2.51	2.60	2.27	2.97	2.99	3.00	
	169	0.89	0.86	SMW	0.88	0.87	0.92	0.87	0.89	0.82	
GWN	175	0.91	0.89		0.91	0.90	0.95	0.90	0.93	0.90	
GVVIV				RTE	0.94	0.88	0.99	0.88	0.86	0.98	
					0.99	0.93	1.02	0.93	0.90	0.98	
	37	1.38	0.83	SMW	0.89	0.88	0.90	1.29	1.17	1.38	
PSU	39	1.45	0.92	SIVIVV	0.97	0.94	0.96	1.44	1.41	1.37	
P30				DTE	1.28	1.33	1.38	1.31	1.32	1.39	
				RTE -	1.32	1.36	1.48	1.51	1.44	1.44	
	106	1.56	1.37	CMM	1.10	1.35	1.15	1.35	1.47	1.56	
CVE	111	1.66	1.41	SMW	1.21	1.43	1.21	1.43	1.58	1.61	
SXF				DTE	1.45	1.43	1.48	1.73	1.71	1.82	
				RTE -	1.48	1.46	1.49	1.77	1.76	1.87	

Table S4. RMSE (in K) for the selected methods of Landsat 8 LST calculation at all SURFRAD stations, with observations divided by NDVI into the bare soil (NDVI < 0.2), mixed surface ($0.2 \le \text{NDVI} \le 0.5$) and vegetation (NDVI > 0.5). The lowest values are highlighted with a grey background.

Subset	N	ST	SMW ASTER		NDVITHM			SNDVITHM		
Subset				-	SO	SK	YU	SK	YU	WA
Bare soil	249	2.71	2.26	SMW	2.29	2.24	2.19	2.29	2.22	2.21
Date Soil				RTE	2.37	2.49	2.74	2.44	2.54	2.56
Mixed	394	4.21	2.74	SMW	2.35	2.58	2.38	2.58	2.69	2.84
surface				RTE	3.55	4.02	3.61	3.97	4.11	4.29
Vegetation	401	3.21	2.55	SMW	2.27	2.27	2.34	2.38	2.40	2.83
vegetation				RTE	2.95	2.95	3.09	3.07	3.09	3.68
All data	882	3.61	2.58	SMW	2.33	2.42	2.33	2.46	2.50	2.70
				RTE	3.13	3.40	3.28	3.39	3.49	3.75